



## **‘Knock on nanocellulose’: Approaching the laminar burning velocity of powder-air flames**

Audrey Santandrea, Marine Gavard, Stéphanie Pacault, Alexis Vignes,  
Laurent Perrin, Olivier Dufaud

### **► To cite this version:**

Audrey Santandrea, Marine Gavard, Stéphanie Pacault, Alexis Vignes, Laurent Perrin, et al.. ‘Knock on nanocellulose’: Approaching the laminar burning velocity of powder-air flames. *Process Safety and Environmental Protection*, 2020, 134, pp.247-259. 10.1016/j.psep.2019.12.018 . hal-03060078

**HAL Id: hal-03060078**

**<https://hal.science/hal-03060078>**

Submitted on 21 Jul 2022

**HAL** is a multi-disciplinary open access archive for the deposit and dissemination of scientific research documents, whether they are published or not. The documents may come from teaching and research institutions in France or abroad, or from public or private research centers.

L’archive ouverte pluridisciplinaire **HAL**, est destinée au dépôt et à la diffusion de documents scientifiques de niveau recherche, publiés ou non, émanant des établissements d’enseignement et de recherche français ou étrangers, des laboratoires publics ou privés.



Distributed under a Creative Commons Attribution - NonCommercial 4.0 International License

**‘Knock on nanocellulose’:**

**approaching the laminar burning velocity of powder-air flames**

Audrey Santandrea <sup>1,2</sup>, Marine Gavard <sup>1</sup>, Stéphanie Pacault <sup>1</sup>, Alexis Vignes <sup>2</sup>, Laurent Perrin <sup>1</sup>, Olivier Dufaud <sup>1,\*</sup>

**\*Corresponding author:** Olivier Dufaud (E-mail address: [olivier.dufaud@univ-lorraine.fr](mailto:olivier.dufaud@univ-lorraine.fr))

<sup>1</sup> Laboratoire Réactions et Génie des Procédés, Université de Lorraine, CNRS, LRGP, F-54000 Nancy, France

<sup>2</sup> INERIS, Accidental Risks Division, Parc Technologique ALATA, BP 2, F-60550, Verneuil-en-Halatte, France

**Abstract:**

Due to their low sedimentation rate, nano-objects offer the opportunity to study flame propagation at low turbulence. The burning velocity was then estimated by flame visualization in two apparatuses: a vertical 1 meter long tube with a square cross-section and a 20L sphere equipped with visualization windows and a vent. This work aims to study the laminar burning velocity of nanocellulose by a direct visualization of the flame propagation within these devices. A high-speed video camera was used to record the flame propagation, and an estimation of the unstretched burning velocity was obtained through linear and nonlinear relationships relating the flame stretching and the flame velocities. Although these methods were initially established for gases, the organic nature of nanocellulose implies a fast devolatilization, which makes the application of the methods possible in this work. Similar results were obtained in both apparatuses in different turbulence conditions, proving the

laminar burning velocity was approached. The laminar burning velocity for the nanocellulose was determined to be  $21 \text{ cm.s}^{-1}$ . This value, estimated through flame propagation visualization, was then compared to the value calculated by applying a semi-empiric correlation to the pressure-time evolution recorded during standard explosion tests in the 20L vessel.

**Keywords:** Dust Explosion; Nanocellulose; Flame propagation; Burning Velocity; Nanopowder

## 1. Introduction

In order to assess explosion risks, the determination of key safety parameters is required (Eckhoff, 2003; Jespen, 2016). Among these parameters, the maximum explosion overpressure and the maximum rate of pressure rise are commonly used to characterize the explosion severity. Their determination implies controlled explosion tests in a closed vessel to measure the pressure evolution with time, which induces a volume-dependence of the results. To be able to design protection equipment, normalized test conditions and apparatuses are then needed. For instance, the EN 14034 standard is generally used, recommending tests in a 20L sphere or a  $1 \text{ m}^3$  vessel under specific conditions (injection procedure, type of nozzle, ignition delay time, ignition source and energy, initial temperature and pressure).

However, standard conditions can be different from industrial conditions (Tamanini, 1990) and do not consider the specificities of each powder. For instance, the ignition energy is set at 10 kJ while the minimum ignition energy can be much lower, which can lead to an overdriving phenomenon and a misestimation of the risk (Going et al., 2000; Zhen and

Leuckel, 1997). Moreover, to represent the volume-dependence of the experimental explosion parameters, a ‘cube-root law’ was proposed by Bartknecht (1989) and demonstrated later by Eckhoff (2003). This law is valid under several assumptions considering that the vessels have similar geometries, the flame thickness is negligible with respect to the vessel radius, the burning velocity is the same in both volumes and point ignition occurs at the center of the vessels (Lewis and von Elbe, 1987; Skjold, 2003). Several tests have been performed to compare results obtained in the 20L sphere and the 1m<sup>3</sup> vessel, revealing significant differences between the two vessels, thus questioning the validity of the cube-root law (Clouthier et al., 2019; Proust et al., 2007; van der Wel et al., 1992). It has notably been proven that radiation can play a significant role in dust combustion, which tends to increase the flame thickness and even invalidate the cube-root law in some cases, especially for metal particles (Bidabadi and Azad, 2015; Dahoe et al., 1996; Taveau et al., 2018). Discrepancies have also been found in terms of turbulence, showing the ignition delay time in both vessels does not allow the same initial turbulence of the dust cloud (Amyotte et al., 1988; Dahoe et al., 2001; Pu et al., 1991; van der Wel, 1993).

If the procedures to determine explosion safety parameters are relatively well defined for micro-powders, they are still subject to debate, especially for nanopowders. Several authors have highlighted, that due to their small size, nanoparticles develop a high specific surface area leading to specific explosion properties (Amyotte, 2014; Boilard et al., 2013; Bouillard et al., 2010; Eckhoff, 2012; Mittal, 2014; Vignes et al., 2019; Wu et al., 2014). Among these specificities, their high specific surface area can both lead to changes in the rate-limiting step of the oxidation reaction (Bouillard et al., 2010; Vignes et al., 2019) and to the modification of the dust cloud particle size distribution due to the agglomeration phenomenon (Eckhoff, 2012; Santandrea et al., 2019a). Moreover, other specificities may call into question the relevance of standardized tests in a closed vessel. For instance, due to their increased ignition

sensitivity, underlined notably by Krietsch et al. (2015), Mohan et al. (2012) and Sundaram et al. (2013), an overdriving or pre-ignition phenomenon is more likely to occur when testing nanopowders. Furthermore, the radiative heat transfer occurring during the flame propagation can be greatly affected by the agglomeration level of the dust cloud (Dufaud et al., 2011; Kosinski et al., 2013; Vignes, 2008). In the case of enhancement of the radiative transfer, the flame thickness would no longer be negligible with respect to the vessel radius, as assumed by the cube-root law. As a consequence, a direct transposition of the safety parameters from lab-scale to industrial-scale may be inaccurate.

To overcome the cube-root law limitations, flame propagation is often studied and used in Computational Fluid Dynamics (CFD) simulations to characterize gas explosion (Di Benedetto et al., 2013; Ghaffari et al., 2019; Skjold, 2003). The essential parameters are then the flame thickness and, more importantly, the laminar burning velocity (Belerrajoul, 2019; Dahoe et al., 2002a). This latter is a fundamental property of the fuel and only depends on the fuel nature and the mixture concentration (Miao et al., 2014). It can be used in simulations to evaluate the consequences of an explosion scenario with controlled conditions (Skjold, 2007; Tolias and Venetsanos, 2018). Although the estimation of the laminar burning velocity of gases is not trivial, the experimental determination of the laminar burning velocity of dust-air mixtures is much more difficult to perform than for gases due to the inherent turbulence related to the powder dispersion. Nevertheless, some experiments have been performed by various authors in a micro-gravity environment during a parabolic flight or using a drop tower (Goroshin et al., 2011; Lee et al., 1993; Pu et al., 1998; Tang et al., 2009). However, such tests being very expensive and difficult to perform on a large scale and with a high frequency, three more accessible methods for the determination of the unstretched burning velocity can be found in the literature: the burner method, with various existing configurations (Dahoe et al., 2002; Julien et al., 2017; Lomba et al., 2019; van der Wel, 1993), the contained explosions

method (Silvestrini et al., 2008; Skjold, 2003; van der Wel, 1993) and the tube method (Andrews and Bradley, 1972; Di Benedetto et al., 2011; Proust, 2006). However, test results obtained in turbulent conditions had to be numerically extrapolated to a zero degree of turbulence (Bradley et al., 1989); as a consequence, the term ‘unstretched burning velocity’ will be preferred to ‘laminar flame velocity’ to qualify the parameter obtained.

Despite the greater accessibility of these methods, experimental issues remain and usually limit the reproducibility and accuracy of the results. In addition to the stochastic nature of turbulence, issues can also come from particle agglomeration, instabilities of the biphasic flow, set-up fouling or flame front visualization difficulties. However, for specific reactive mixtures such inconveniences may be limited: for instance, testing gas-dust mixtures with a low dust concentration (called gas-driven hybrid mixtures) in a semi-open tube allowed the determination of their unstretched flame velocity and highlighted the influence of turbulence/combustion interactions on the flame propagation (Cuervo, 2015; Torrado et al., 2017b).

Similarly, the low inertia of nanoparticles allows tests with a long ignition delay time. Consequently, experiments can be performed at low turbulence with nanoparticles while sedimentation would occur for micropowders under the same experimental conditions. Decreasing the turbulence level of the initial dust cloud can help approaching the ‘laminar flame velocity’ of dust-air mixtures through the assessment of an unstretched flame velocity, which is then expected to be independent from turbulence. This concept will be developed through the characterization of the unstretched burning velocity of a nanocellulose powder using three different procedures and set-ups: a semi-opened tube, a vented vessel and the classical 20L explosion sphere.

## 2. Materials and methods

### 2.1. Nanocellulose characterization

In this study, an organic powder was chosen with regard to experimental, scientific and industrial considerations. First of all, the powder should display a sufficient ignition sensitivity to be ignited by an electrical spark and thus ensure a single point ignition, which is not the case of carbonaceous powders (Turkevich et al., 2016; Vignes, 2008). Moreover, metal nanopowders may be subjected to pre-ignition and their flame tend to propagate with a significant thermal radiation, which can hinder the flame front observation. Organic nanopowders, with a minimum ignition energy of a few millijoules and a flame propagation with limited thermal radiation, then appears to be a good solution. Moreover, during their combustion, the devolatilization step occurs rapidly, which can lead to flame propagation rather similar to those already observed for gas-powder hybrid mixtures (Cuervo, 2015) or flame propagation occurring in the gas phase (Bradley and Lee, 1984) and makes possible the application of relations initially established for such mixtures.

From an industrial point of view, nanocellulose is of increasing interest due to its specific chemical and physical properties providing a wide variety of applications, notably in photonics, medical devices, coating, electronics, 3D printing and plastics (Abitbol et al., 2016). The powder used in this study is a cellulose nanocrystals powder (NCC from CelluForce) with primary fiber dimensions of 3 nm width, an average length of 70 nm and a specific surface area of  $400 \text{ m}^2.\text{g}^{-1}$ , as specified by the producer (CelluForce, 2016). Although this powder is constituted of nanofibers, the word “nanoparticles” will be employed in this work with no distinction between fibers and particles. The nanocellulose was dried at  $90^\circ\text{C}$  under vacuum before performing tests to limit the influence of humidity on the explosion parameters and improve reproducibility. Nanocellulose was observed by Scanning Electron Microscopy (Figure 1) but did not reveal clearly the nanometric structure of the powder.

Additional experiments were performed with a rotative drum combined with a Condensation Particle Counter (CPC – TSI 3007) and demonstrate the presence of two modes at 2  $\mu\text{m}$  and 20 nm. Further tests were performed directly after powder dispersion in the explosion vessels in order to highlight the presence of primary nanopowders in addition to the inevitable agglomerates.

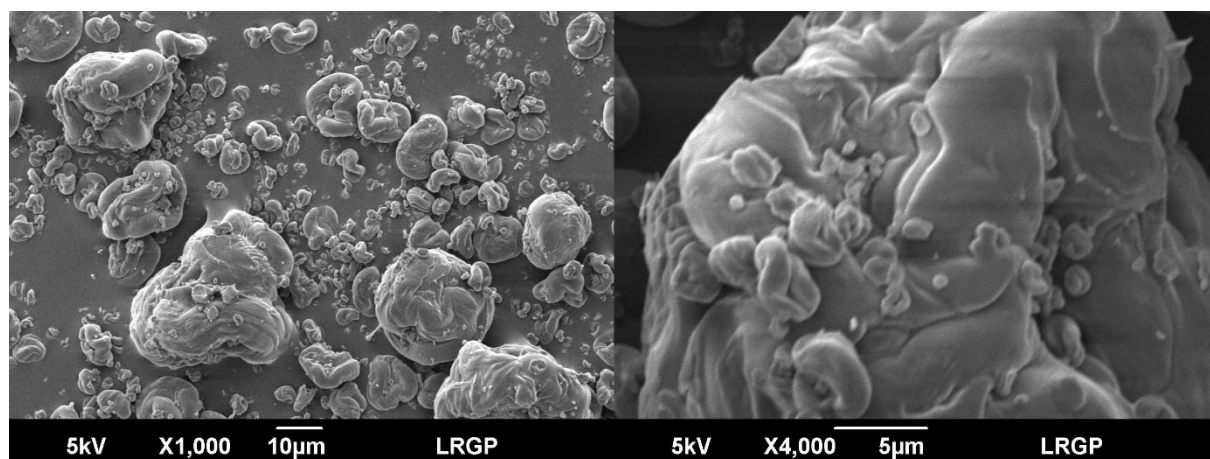


*Figure 1 Nanocellulose observed with an Scanning Electron Microscope*

## 2.2. Explosion tests equipment

The unstretched burning velocity of nanocellulose was estimated using three experimental methods. First, a flame propagation tube of 7 x 7 x 100 cm<sup>3</sup> open at its upper end and implementing the ignition system of the modified Hartmann tube, was coupled with a high-speed video camera at 4000 fps with 240  $\mu\text{s}$  of exposure time (Phantom V9.1). Electrodes are located at 12.5 cm from the bottom of the tube. The equipment and procedure are fully described by Cuervo et al. (2017) and Torrado et al. (2017) who validated the set-up and procedure with methane and obtained encouraging results for hybrid mixtures. However, the small volume, especially around the ignition zone, implies that the flame is influenced by the walls quite soon after the ignition, which impacts its propagation. Therefore, the analysis is limited to the first moments of the flame kernel growth, between ignition and the flame spatial



acceleration (or quenching) due to the presence of the wall. Consequently, a second method was developed to study flame propagation within a modified 20L sphere.

The standard apparatus described by European standards (EN 14034-1, 2004; EN 14034-2, 2006) does not allow a clear visualization of the content of the sphere, preventing the observation of both the dust cloud after dispersion and the flame propagation. To overcome this limitation, Murillo (2016) designed a new 20L sphere equipped with four visualization windows made of borosilicate with a diameter of 9.7 cm on the lateral sides and one on the top to characterize the dust cloud in terms of particle size distribution and turbulence. Torrado (2017) adapted the apparatus to perform hybrid mixtures explosion tests and to study the flame propagation. Therefore, a lateral window was removed to integrate an ignition source composed of two tungsten electrodes connected to a KSEP 320 system (Kühner AG - 15 kV / 15 mA, i.e. 225 W) generating a permanent spark whose duration, and thus energy, can be varied. A modification of the Kühner software was necessary to control accurately the ignition delay time, called 'tv', when using the permanent spark. A pressure relief valve, opening at 1.15 atm (abs), was added on top of the sphere to protect the windows during the explosion. The flame front and shape are imaged using a Schlieren system, combined with the high-speed camera. The Schlieren setup consists of a 150 W xenon lamp (66475-150XV-R22 Xenon Light Source) equipped with a lens, a pinhole with a diameter of 1 mm to obtain a single-point light source, and a spherical mirror reflecting the punctual light toward a filter placed in front of the camera (Figure 2). This technique, notably described by Mazumdar (2013), allows the observation of density variations, which provides a better visualization of the flame front.

The results obtained with both apparatuses were then compared to the correlations established by Silvestrini et al. (2008), based on the evolution of the maximum overpressure and the maximum rate of pressure rise during an explosion carried out in a closed vessel. To ensure a

proper comparison, explosions tests were performed in the standard 20L sphere with a permanent spark to avoid an overdriving phenomenon and a source ignition dependence of the results. Tests were also performed on nanocellulose according to the standard procedure (EN 14034-1:2004 + A1:2011; EN 14034-2: 2006 + A11:2011) and 10 kJ chemical igniters. The tube tests were performed at 300 mJ and in the 20L sphere, open and closed, an energy of 10J was used, knowing the minimum ignition energy of the chosen dried nanocellulose for those experiments is about 5 mJ as measured in a Mike 3 apparatus.

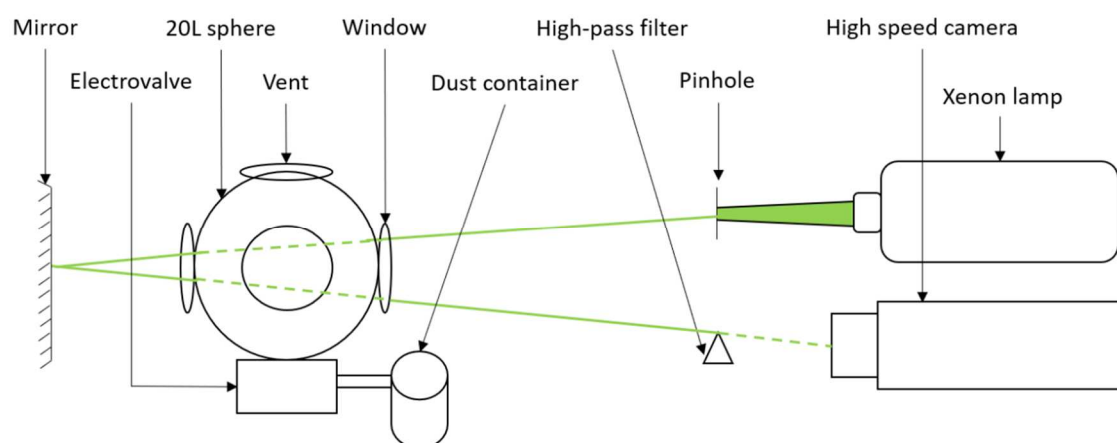


*Figure 2. Schematic of the Schlieren setup and the modified 20L sphere*

### 2.3. Dust cloud characterization

The particle size distribution of a dust cloud constituted of nanoparticles is one of the most important factors influencing the flame propagation but also one of the most complex to consider. Indeed, no apparatus or technique currently allows the determination at high frequency and high concentration, i.e. a concentration equal or greater than the usual minimum explosive concentrations ( $125 \text{ g.m}^{-3}$  for the chosen nanocellulose), over a whole range of particles sizes from 10 nm up to 200  $\mu\text{m}$ .

To characterize the dust cloud, a laser diffraction sensor (Sympatec) was used through the visualization window of the 20L sphere and the tube to measure the in-situ particle size distribution (PSD) for particle sizes from 0.5 to 175  $\mu\text{m}$  (R3 lens) at a frequency of 2 analyses per millisecond. Since the combustion reaction can occur at the surface of the particles, as a function of the reaction regime considered, the surface fraction is considered instead of the usual volume fraction for the particle size distribution. It should be noted that other metrics, such as the volume or number can also be considered to represent the particle size distribution (Santandrea et al., 2019b).

In addition, the turbulence level of the dust cloud estimated by Dahoe et al. (2001) using a laser Doppler anemometer was considered in the 20L sphere, and the measurements performed by Particle Image Velocimetry (PIV) by Cuervo (2015) were used to estimate a root-mean square velocity  $u_{\text{rms}}$  of the dust cloud in the flame propagation tube. Regarding the values presented in Table 1, it appears that the turbulence level is always higher in the 20L sphere than in the propagation tube, which is due to the high pressure applied during the injection in the sphere and to the use of a dust canister. However, for both equipment, the turbulence level decreases rapidly in the low ignition delay time range (from 60 to 120 ms, 71% lower in the 20L sphere and 39% in the tube) and seems to stabilize for high ignition delay times ( $<200$  ms), as discussed by Murillo et al. (2018) and Santandrea et al. (2019a). Indeed, between 100 ms and 200 ms, the root-mean square velocity decreases 67% in the 20L sphere and 60% in the tube, and only 14% in the 20L sphere and 25% in the tube between 300 ms and 400 ms. This “stable stage” allows to reach pseudo-laminar conditions and to approach a laminar burning velocity when increasing sufficiently the ignition delay time.

*Table 1. Root mean square velocities measured in the 20L sphere and in the propagation tube (Cuervo, 2015; Dahoe et al., 2001)*

Ignition delay time (ms)	$u_{rms}$ in the 20L sphere ( $m.s^{-1}$ ) (Dahoe et al., 2001)	$u_{rms}$ in the propagation tube ( $m.s^{-1}$ ) (Cuervo, 2015)
60	3.5	1.4
100	1.5	1.0
200	0.5	0.4
300	0.35	0.2
400	0.3	0.15

231

232 Explosion tests in the standard closed 20L sphere were performed according to EN 14034-  
233 1:2004 + A1:2011 and EN 14034-2:2006 + A11:2011 on the nanocellulose and on  
234 microcrystalline cellulose (Avicel,  $d_{50} = 108 \mu m$ ) for comparison.

#### 235 2.4. Assessment of unstretched flame velocity for nanopowders

236 The determination of the unstretched flame velocity was performed both by direct  
237 visualization of the flame propagation and by analyzing the pressure-time curves recorded  
238 during an explosion in the 20 L sphere.

##### 239 2.4.1. Flame propagation experiments

###### 240 2.4.1.1. Flame propagation and stretching observation

241 The propagation speed can be estimated using existing mathematical models based on several  
242 hypotheses (Chen and Ju, 2007; Frankel and Sivashinsky, 1984; Joulin and Clavin, 1979).  
243 The flame is then assumed to be spherically expanding and governed by an overall one-step  
244 exothermic reaction, and the thermodynamic properties of the mixture such as the molecular  
245 weight, the specific heat and the thermal conductivity are considered constant. The potential  
246 heat losses are neglected and the combustion process is assumed to be isobaric, which seems  
247 reasonable before the flame is affected by the vessel walls. With all these hypotheses, the  
248 laminar burning velocity can be estimated using a linear or a non-linear methodology, from  
249 the knowledge of the turbulent burning velocity and flame stretching.

To evaluate those parameters, flame propagation videos were analyzed by a model developed by Cuervo (2015) in MatLab's Simulink using the Vision toolbox (Cuervo et al., 2017; Torrado et al., 2017). This model isolates the flame profile for each frame of the video as shown in Figure 3 and calculates the position of the flame front  $z$ , the estimated cross-section area  $A_s$  and the estimated flame surface  $A_f$ . In the case of flame kernels growing spherically, the flame radius is generally considered to estimate the spatial velocity (Law, 2006; Varea, 2013). However, since the flame kernel appears to grow as an ellipsoid at low turbulence levels, the spatial velocity is calculated by deriving the position of the front flame.

Since the laminar flame velocity is independent of the vessel geometry and size, only the phase of 'free' flame kernel propagation is considered, i.e. when the flame is not significantly affected by the vessel walls, by compression or gas-wall heat transfers. It should be noted that, due to the contribution of the ignition source and the small size of the initial flame kernel, which can be located –with respect to the camera- behind unburnt particles, the very first milliseconds of the videos are also often delicate to analyze. The position of the flame  $z$  being known for different times, the spatial velocity of the flame  $S_s$  can be deduced. Then, the flame burning velocity  $S_u$  can be calculated using Andrews and Bradley (1972) formula:

$$S_u = S_s \frac{A_s}{A_f} \quad (1)$$

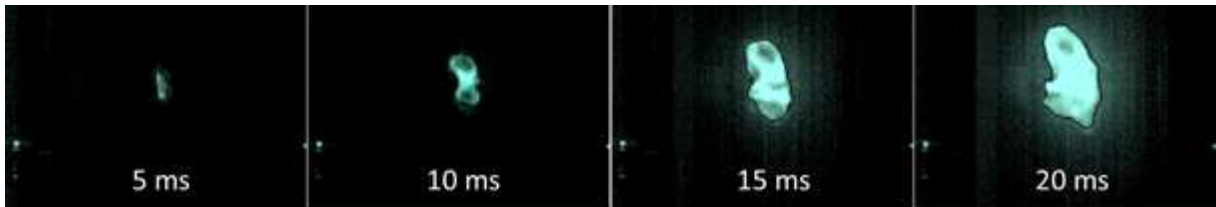


*Figure 3. Time evolution of the flame profile in the semi-open tube for a dispersion of 500 g.m<sup>-3</sup> of nanocellulose at 340 ms ignition delay time*

271

272 This model is valid if the flame burning velocity  $S_u$  remains constant (which essentially  
273 means that the local fuel equivalence ratio does not change during the flame propagation), if  
274 the flame thickness is small in comparison to the flame curvature and if the spatial velocity  $S_s$   
275 is uniform over the whole surface of the flame. However, in the context of these experiments,  
276 the ignition is performed 12.5 cm above the closed side of the tube, implying the hot burnt  
277 gases are pushing up the fresh gases due to their thermal expansion. Therefore, a thermal  
278 expansion factor  $\chi$ , represented by the ratio between the temperatures of the hot burnt gases  
279 and the initial cold gases, should be introduced to correct this increased velocity. The  
280 temperature of the gases generated by the combustion reaction is approximated to be the  
281 adiabatic temperature at equilibrium conditions and is determined by the CEA software  
282 (McBride and Gordon, 1996). Equation (1) then becomes:

$$283 \quad S_u = \frac{S_s A_s}{\chi A_f} \quad (2)$$

284 However, as previously explained, only the “free” flame kernel propagation is considered,  
285 meaning the analysis is stopped when the flame is close to the walls but is still unaffected by  
286 their presence. This induces that, at this early stage, the flame kernel growth is unaffected by  
287 the thrust of the gases against the bottom of the tube and by the pressure increase taken into  
288 account by the thermal expansion factor.

289 It should be underlined that the burning velocity of a fuel-air mixture depends on the initial  
290 dust concentration, the pressure and the temperature, but also the turbulence. More than any  
291 other parameter, this point is very important and specific to dust explosions due to the  
292 inherent turbulence developed when generating the dust cloud. This effect can be estimated  
293 using the flame’s stretching factor  $K$ , called Karlovitz factor (Karlovitz et al., 1951), defined  
294 as:

$$K = \frac{1}{A_f} \frac{dA_f}{dt} \quad (3)$$

The sign of the Karlovitz factor indicates the expansion (K positive) or compression (K negative) of the flame surface area. Since the stretching can be due to the curvature of the flame or to the strain rate of the flow, the stretching factor can be decoupled in two different variables  $K_c$  and  $K_s$  (Bradley, 2000). However, in this work, the flame stretching will be considered as a single phenomenon combining both effects.

In the literature, two relations to link the Karlovitz factor to the burning velocity are mainly used by considering the assumptions previously mentioned: a linear relation and a non-linear one. Although those relations were initially established for gases, Cuervo et al. (2017) and Torrado et al. (2017) obtained encouraging results by applying them to starch/methane as well as carbon nanoparticles/methane hybrid mixtures. In this work, the same relations are applied to pure dust explosions. Indeed, the low inertia of nanocellulose particles allows the measurement at very low turbulence, leading to a spherical/ellipsoidal flame kernel growth. Moreover, the organic nature of the chosen powder induces a fast devolatilization which implies that, under certain concentration and turbulence conditions, the dust combustion would be controlled by gas combustion (Di Benedetto and Russo, 2007).

#### 2.4.1.2. Linear relation

Most of the authors studying flame propagation and laminar burning velocity (Cuervo et al., 2017; Dahoe et al., 2002; Di Benedetto et al., 2011) use a linear relation established for pure gases and stating that, in a first approach, the Karlovitz factor can be linked to the flame burning velocity by the following relationship (Clavin, 1985; Markstein, 1964):

$$S_u = -\delta_M K + S_u^0 \quad (4)$$

where  $S_u^0$  is the unstretched burning velocity and  $\delta_M$ , the Markstein length, whose sign provides an indication on the stability of the flame (Clavin, 1985). This linear relation is valid if the flame stretching is weak, i.e. if the Karlovitz number is low, and if the ratio of thermal diffusivity to mass diffusivity, called the Lewis number, is equal to unity.

#### 2.4.1.3. Non-linear relation

Even if the linear relation has been extensively adopted in various studies concerning flame propagation (Beckmann et al., 2019; Bradley et al., 2019; Ichikawa et al., 2019; Torrado et al., 2017), it has some limitations (Petersen and Emmons, 1961). Indeed, this relation is less accurate for Lewis numbers different from unity (Tien and Matalon, 1991) and if the flame stretching level is high, which corresponds to great values of the Karlovitz factor (Vagelopoulos et al., 1994). As a consequence, some authors developed and applied a nonlinear relation to link the unstretched flame velocity to the flame stretching of gaseous mixtures (Buckmaster, 1977; Halter et al., 2010; Kelley and Law, 2009; Sivashinsky, 1975):

$$\left(\frac{S_u}{S_u^0}\right)^2 \cdot \ln\left(\frac{S_u}{S_u^0}\right)^2 = -\frac{2\delta_M K}{S_u^0} \quad (5)$$

The previous analysis was applied along with relations 4 and 5 to the experimental data recorded during flame propagation in the semi-open tube and in the vented 20L sphere.

#### 2.4.1.4. Estimation of the unstretched burning velocity

An illustration of the evolution of the burning velocity with the Karlovitz factor is presented in Figure 4 for a concentration of 500 g.m<sup>-3</sup> of nanocellulose. It appears that both relations seem to match approximately the experimental data. In this example, the unstretched flame velocity obtained using the linear relation is  $20.5 \pm 0.6 \text{ cm.s}^{-1}$  and  $21.3 \pm 0.6 \text{ cm.s}^{-1}$  using the nonlinear relation proving a good consistency between both methods. It should be noted that the average discrepancy between the flame velocities obtained by both methods is 4 %, which



means that there is no statistical difference between the methods. However, it appears in Figure 4 that the scattering of data is far from being negligible, which is notably due to uncertainties in the flame surface determination at each step of the propagation and hinders sometimes the application of such correlation.

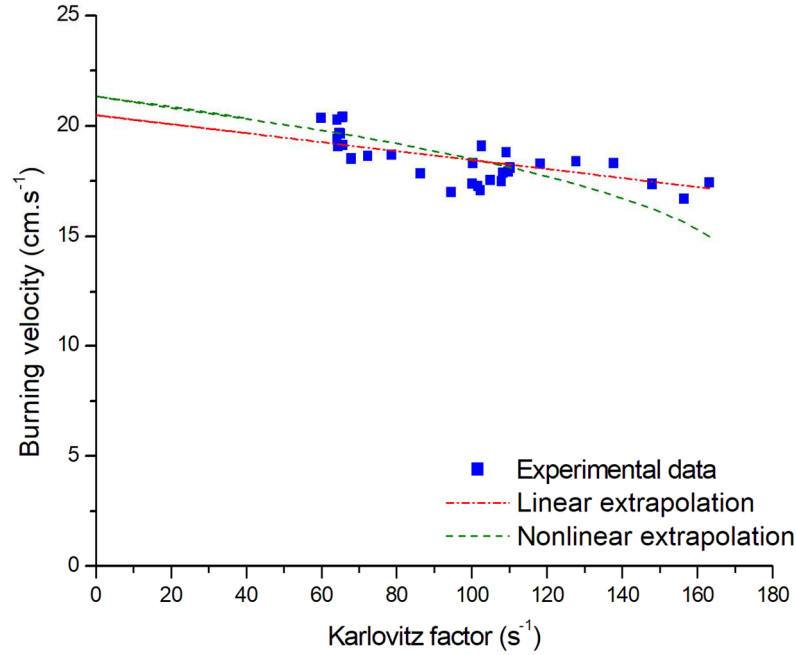


Figure 4. Illustration of the burning velocity – stretching factor relation for a  $500 \text{ g.m}^{-3}$  nanocellulose-air mixture for  $t_v = 340 \text{ ms}$

Since the derivation process used to determine the Karlovitz factor and the spatial velocity can induce some uncertainties, the time evolution of the position of the flame front, the flame area and cross-section was systematically smoothed based on a second order polynomial as shown in Figure 5 to obtain a general trend and avoid local discontinuities. The coefficient of determination is systematically at least 0.99, showing a good agreement with the experimental results.

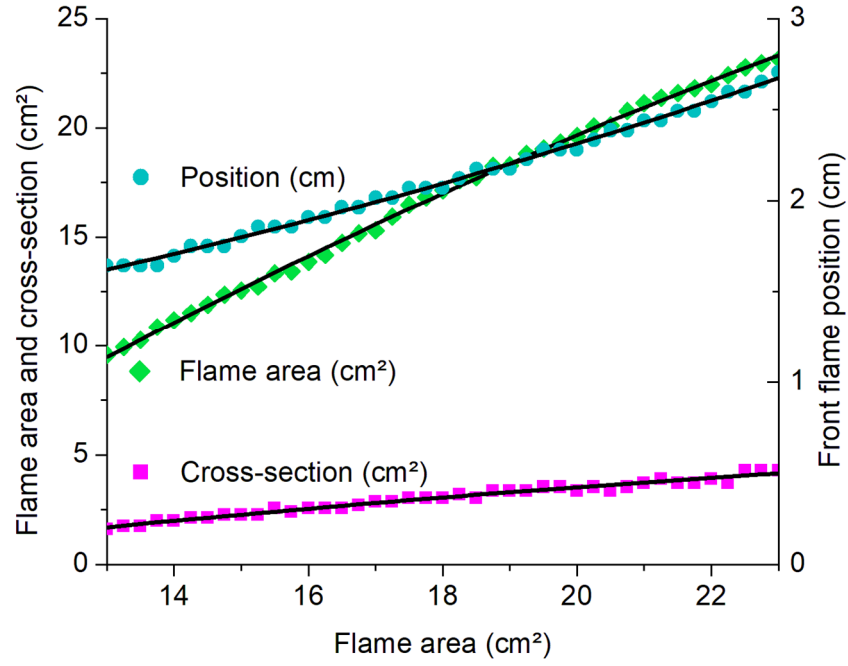


Figure 5. Evolution of the front flame position, flame area and cross-section with time for a  $500 \text{ g.m}^{-3}$  nanocellulose-air mixture for  $t_v = 340 \text{ ms}$

Figure 6 then represents the evolution of the burning velocity with the stretching factor after data smoothing, showing a better agreement with the different theoretical relationships than the initial raw experimental data. Indeed, the unstretched burning velocity now reaches  $23.1 \pm 0.3 \text{ cm.s}^{-1}$  with a coefficient of determination of 0.95 instead of 0.36 in the previous case with the linear fitting, and it reaches  $21.8 \pm 0.4 \text{ cm.s}^{-1}$  using the nonlinear fitting. Since the smoothing provides results with a better accuracy, it was systematically realized during the videos analysis phase.

Videos of the explosion occurring in the flame propagation tube and in the vented 20L sphere were then analyzed according to the method described in 2.4.1 and the unstretched burning velocity was estimated using both linear and nonlinear relations.

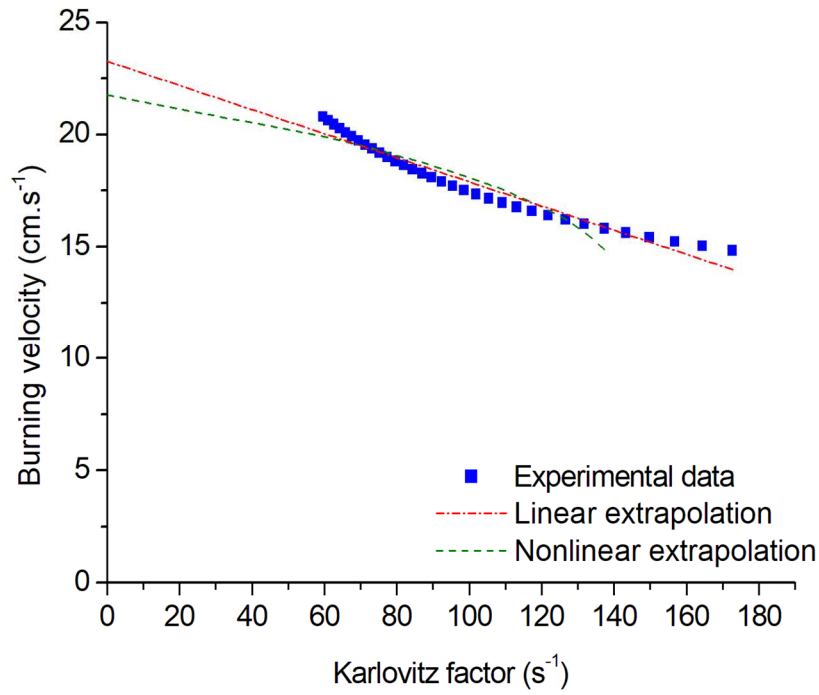


Figure 6. Illustration of the burning velocity – stretching factor relation after smoothing for a 500 g.m<sup>-3</sup> nanocellulose-air mixture for  $t_v = 340$  ms

#### 2.4.2. Pressure-time evolution interpretation

An alternative way to estimate the unstretched burning velocity is provided through the recording of the pressure evolution during an explosion in the 20L sphere. Indeed, some authors such as Silvestrini et al. (2008) developed some correlations between the unstretched burning velocity and the parameters  $K_{St}$  and  $P_{max}$  obtained in the 20L sphere. The results obtained by analyzing the flame propagation will be compared to the ones calculated from the following semi-empiric correlation defined by Silvestrini et al. (2008):

$$S_u^0 = 0.11 \frac{K_{St}}{P_{max} \left( \frac{P_{max}}{P_0} \right)^{0.14} \left( \frac{P_{max}}{P_0} \right)^{\left( \frac{1}{\gamma} \right)}} \quad (6)$$

where  $P_0$  is the atmospheric pressure and  $\gamma$  the ratio of specific heats. As the previously defined relations, this correlation is based on several assumptions, such as the spherical

expansion of the flame and the neglecting of the turbulent length scales. Moreover, the establishment of this correlation based on other existing relations also relying on hypotheses, like a laminar flow or the fact that the burnt gases are trapped behind the expanding flame front, meaning the thermal expansion factor is considered (Harris, 1983). Furthermore, the explosivity index  $K_{St}$  is mentioned in the correlation, meaning that the “cube-root” law and its related hypotheses were used. For instance, the flame front is considered to be a thin reaction zone as defined by Dahoe et al. (1996), and Silvestrini et al. (2008) considered that  $P_{max}$  was defined as the maximum overpressure for a single explosion experiment and that a  $K_{st}$  parameter can be defined from a test performed at a single dust concentration and not from tests performed over a wide range of concentration. Thus, the following relation was applied during this work:

$$S_u^0 = 0.11 \frac{\left(\frac{dP}{dt}\right)_m V^{1/3}}{P_m \left(\frac{P_m}{P_0}\right)^{0.14} \left(\frac{P_m}{P_0}\right)^{\left(\frac{1}{\gamma}\right)}} \quad (7)$$

The unstretched burning velocity of nanocellulose was then estimated using those three methods to test the strengths and weaknesses of each method and ensure the consistency of the methods by identifying a reliable value of the laminar burning velocity.

### 3. Results and discussion

#### 3.1. Particle size distribution of the dust cloud

When characterizing the dust cloud, it first appears that the particle size distribution in the sphere seems to be more monodisperse than in the tube due to the high shear stress occurring during the injection of the powder and potentially breaking the agglomerates of a few micrometers (Figure 7). Although particles with a diameter lower than 0.5  $\mu m$  seem to be present in the flame propagation tube and probably in the sphere, they are not measured directly with this lens.

Similar tests were also performed with the same sensor equipped with a R1 lens (from 0.1 to 35  $\mu\text{m}$ ). In addition, the PSD of the dust clouds was investigated using a Fast Mobility Particle Sizer (FMPS) and a Scanning Mobility Particle Sizer (SMPS) to specifically measure particles with diameters lower than 500 nm in the 20L sphere. It should be underlined that such apparatuses allow the determination of the electrical mobility distribution of the dust cloud. Although it is impossible with those methods to directly compare the PSD of the dust in the sphere and the tube, these experiments clearly confirm the presence of nanoparticles after dispersion in both equipment with dimensions ranging from 100 to 300 nm (with peaks at 150 nm).

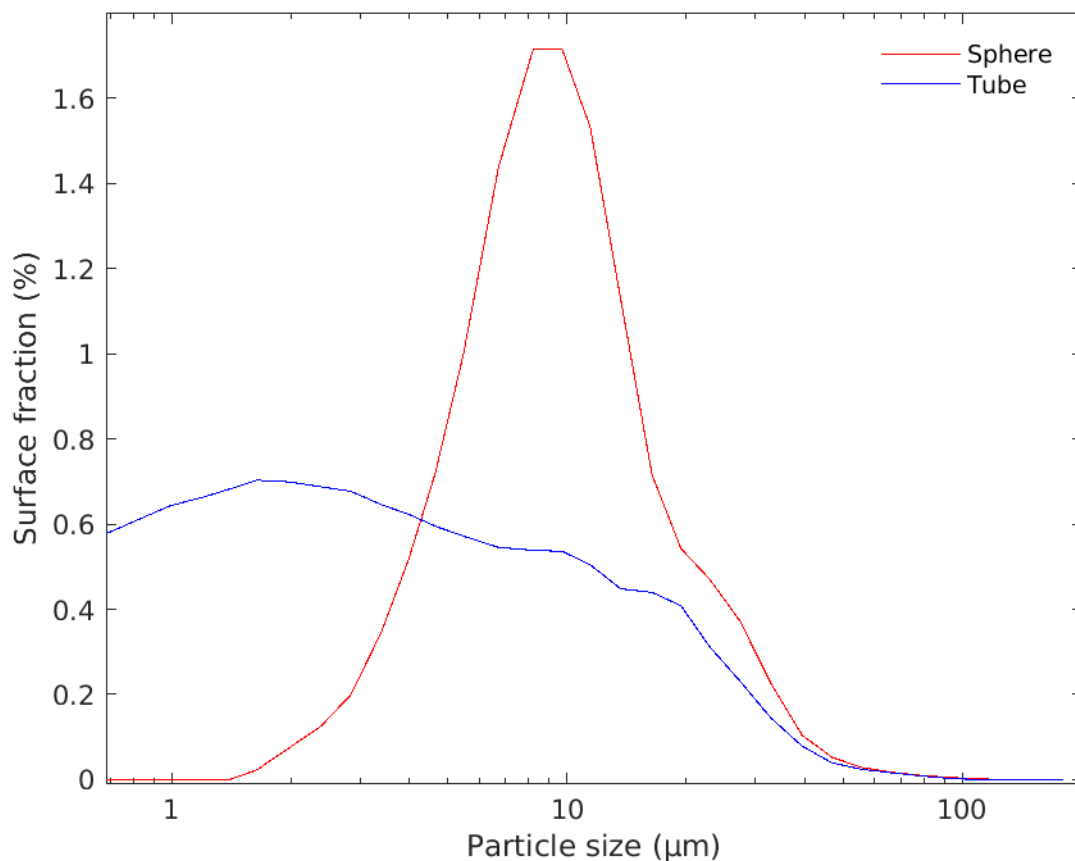


*Figure 7. Evolution of the particle size distribution of nanocellulose agglomerates 200 ms after dispersion in the 20L sphere and in the tube at the ignition location*

### 3.2. Explosion severity of micro and nanocellulose

Before proposing an alternative method for dust explosivity assessment, the standard test method (EN 14034) was applied to compare the explosion severity of micro and nanocellulose. It can be observed that the maximum overpressure  $P_m$  (Figure 8a) of the nanocellulose is slightly greater than that of microcrystalline cellulose, but that the overall behavior of this parameter as a function of the dust concentration is rather similar for both compounds. However, the difference is more significant with respect to the maximum rate of pressure rise  $(dP/dt)_m$  (Figure 8b), which can be explained by the variation of particle size and of specific surface area, which greatly impacts the reaction kinetics. The  $K_{st}$  parameter, obtained through the application of the cubic law, reaches  $135 \pm 3 \text{ bar.m.s}^{-1}$  for nanocellulose at  $1000 \text{ g.m}^{-3}$ , whereas it reaches only  $86 \pm 10 \text{ bar.m.s}^{-1}$  at  $1500 \text{ g.m}^{-3}$  for microcrystalline cellulose.

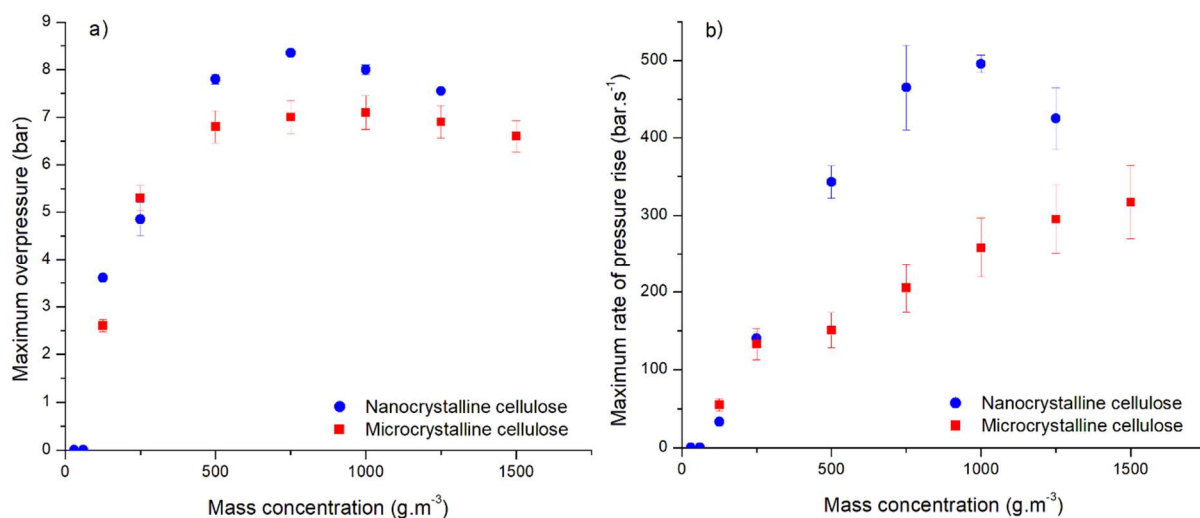
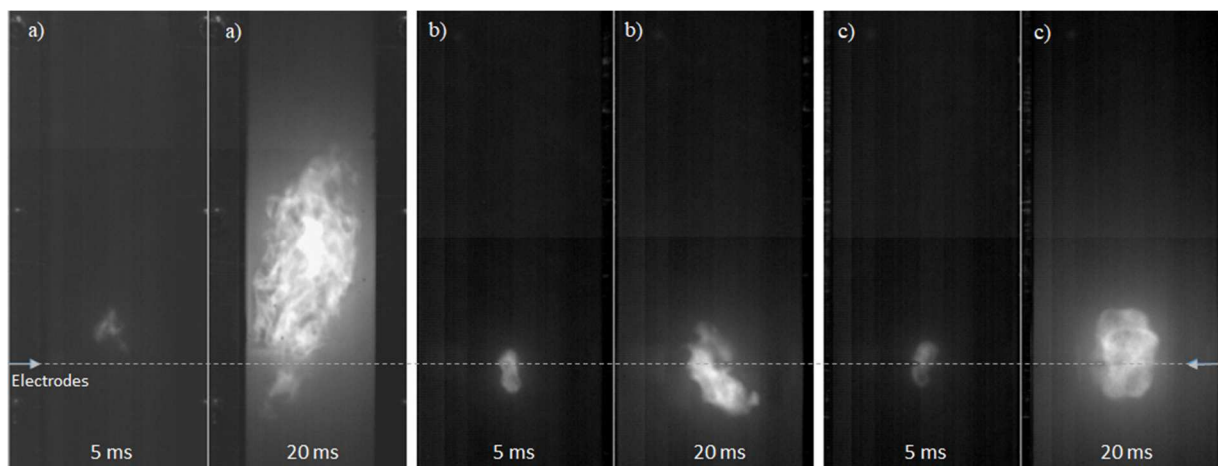


Figure 8. a) Maximum overpressure and b) maximum rate of pressure rise of nanocellulose and microcellulose in standard test conditions

### 3.3. Determination of the optimal operating conditions for flame propagation tests

Explosion tests were first performed at different ignition delay times and at a single concentration of  $500 \text{ g.m}^{-3}$ , estimated in the tube by considering the dust weight and an average dispersion height of 0.35 cm. This concentration is close to the stoichiometric

concentration (around  $250 \text{ g.m}^{-3}$ ) and ensures a visualization of the flame kernel without interference coming from the particles, which occurs with larger concentrations. At high turbulence, i.e. at an ignition delay time lower than 200 ms, the flame kernel grows up rapidly with stretching and is rapidly influenced by the walls (Figure 9a). As a consequence, only a few milliseconds of the video are suitable for the analysis, and the flame profile is difficult to identify due to the turbulence. When slightly reducing the turbulence, the flame kernel growth is slower, but the turbulence level remains too decisive ( $u_{\text{rms}} > 1 \text{ m.s}^{-1}$ ) to precisely define the flame profile (Figure 9b). At very low turbulence, the flame kernel growth is still slow and nearly spherical, showing a behavior similar to that of gases, i.e. a rather smooth flame surface and a flame front with a paraboloidal shape (Figure 9c). It is then possible to correctly identify the flame profile, with 10 to 20 ms of video which can be confidently analyzed. Moreover, it can be noticed that the flame kernel does not move when growing, which shows that it is barely affected by the dust cloud inertia or by the burnt gases thrust. As a result of these observations, ignition delay times from 300 ms to 450 ms, due to a limitation of the apparatus, were considered in the tube and in the 20L sphere for the analyses.



*Figure 9. Visualization of flame propagation of  $500 \text{ g.m}^{-3}$  of nanocellulose in the tube 5 ms and 20 ms after ignition for different ignition delay times (a) 125 ms (b) 235 ms (c) 450 ms.*

Figure 10 presents the results obtained in the flame propagation tube and in the open 20L sphere at different ignition delay times, calculated by linear and nonlinear relations. It appears in Figure 10a that unstretched burning velocities between 18 and 23 cm.s<sup>-1</sup> are obtained using the linear equation and that velocities ranging between 17.5 and 26 cm.s<sup>-1</sup> are obtained with the nonlinear relation, which remains in the same order of magnitude. Both methods lead to similar values, even if the dispersion of the experimental data seems to be more significant in the case of the nonlinear equation. Moreover, Figure 10b shows that the analytical uncertainties are higher when applying the nonlinear relationship to the experimental data measured in the open 20L sphere.

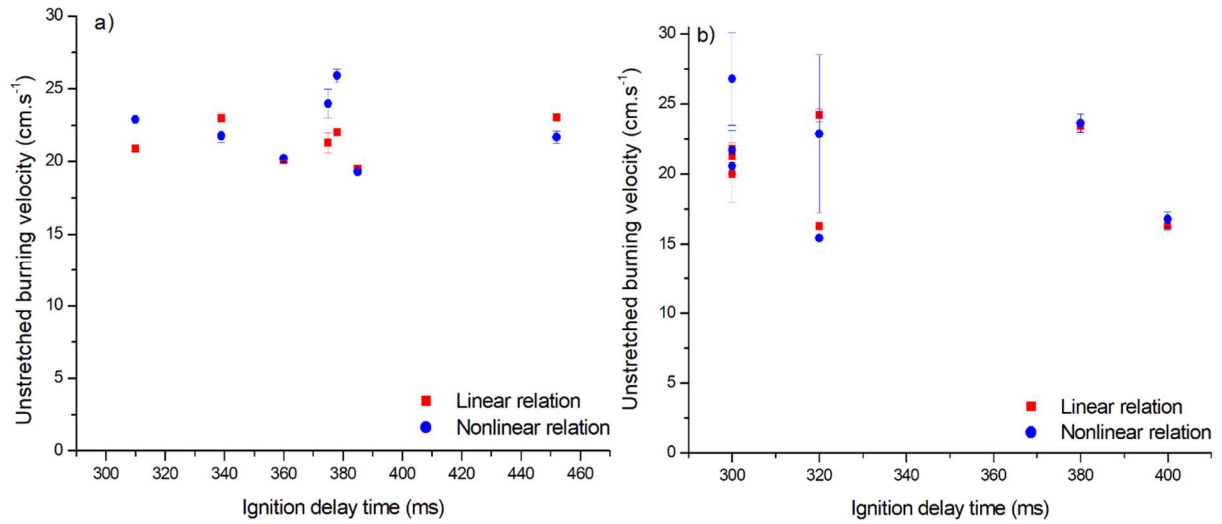


Figure 10. Evolution of the unstretched burning velocity of 500 g.m<sup>-3</sup> of nanocellulose with ignition delay time calculated by the linear and nonlinear relations in a) the propagation tube  
b) the open 20L sphere



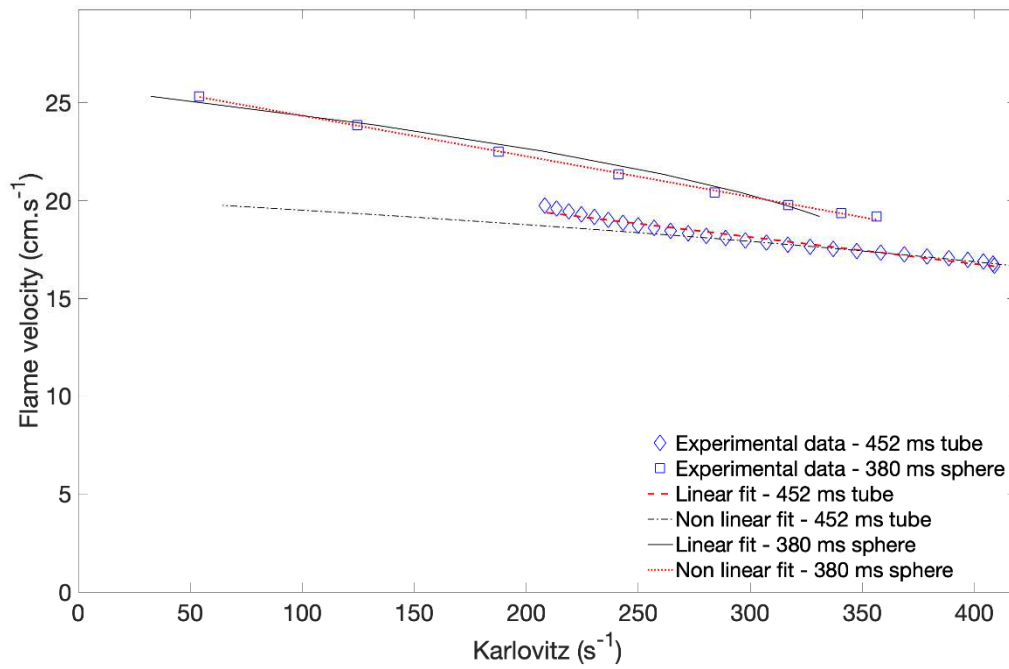
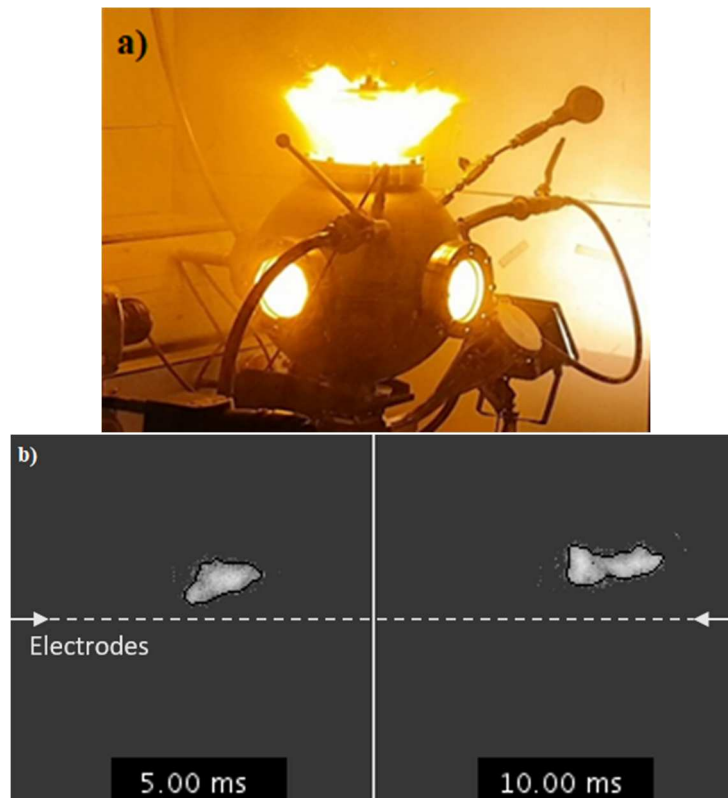


Figure 11. Comparison of the application of linear and nonlinear methods to a nanocellulose explosion:  $500 \text{ g.m}^{-3}$  concentration,  $t_v=452 \text{ ms}$  – tube and  $t_v=380 \text{ ms}$  – vented sphere

Figure 11 shows that the application of the nonlinear relationship is more relevant for the experimental data corresponding to the high-stretch region (from 270 to  $400 \text{ s}^{-1}$ ) of the flame propagation in the tube. However, this zone corresponds to a period of time during which the flame propagation may still be affected by the ignition (near  $400 \text{ s}^{-1}$ ). In most cases, as for instance for the other experimental set of data presented in Figure 11 (380 ms in the open sphere), the linear fit will be preferred to the nonlinear model, especially at low stretching rates. It can also be observed in Figure 11 that the number of experimental points selected for the analysis is often reduced in the case of the open sphere. Indeed, with regard to the tube, the larger volume of the 20 L open sphere is both an advantage and a drawback: an advantage because it reduces the wall effects and a drawback because, during the very first moments of the flame kernel growth, the thickness of the unburnt cloud located between the ignition zone

and the window is great, which hinders the flame visualization and sometimes reduces the ‘analyzable duration’ of the video down to 5 ms. This limitation can be partially overcome by using a Schlieren system, as presented in paragraph 2.2. An explosion in the 20L sphere and the dust kernel 5 ms and 10 ms after ignition of  $500 \text{ g.m}^{-3}$  of nanocellulose are presented in Figure 12a and Figure 12b respectively. In view of the experimental uncertainties and the slight discrepancies between the non-linear and linear relationships, only the results obtained by the latter method will be now considered.



*Figure 12. a) Explosion in the open 20L sphere and b) visualization of the flame kernel 5 ms and 10 ms after ignition of  $500 \text{ g.m}^{-3}$  of nanocellulose and ignition delay time of 300 ms*

### 3.4. Estimation of the laminar burning velocity

Since the turbulence intensity is different in the tube and in the sphere, results were plotted as a function of the root mean square velocity measured in both equipment by Particle Image

Velocimetry. Figure 13 then shows that a very low turbulence level, from 0.21 to 0.13  $\text{m.s}^{-1}$  is reached in the tube, whereas it reaches a minimum of 0.3  $\text{m.s}^{-1}$  in the 20L sphere. However, similar values of unstretched burning velocity are obtained, from 19 to 23  $\text{cm.s}^{-1}$  in the tube and from 16 to 24  $\text{cm.s}^{-1}$  in the sphere. This is due to the fact that, when increasing the ignition delay time, the turbulence level decreases in both equipment until it reaches a region in which the decay is small, as mentioned in paragraph 2.3. This region is observed from 200 ms in both equipment, corresponding to a root-mean square velocity of 0.4  $\text{m.s}^{-1}$  in the propagation tube and 0.5  $\text{m.s}^{-1}$  in the 20L sphere. The flame propagation tube seems to produce more clustered values, which can be explained by the better visualization of the flame kernel providing a longer analyzable video than in the vented 20L sphere, thus a more accurate analysis of the flame propagation.

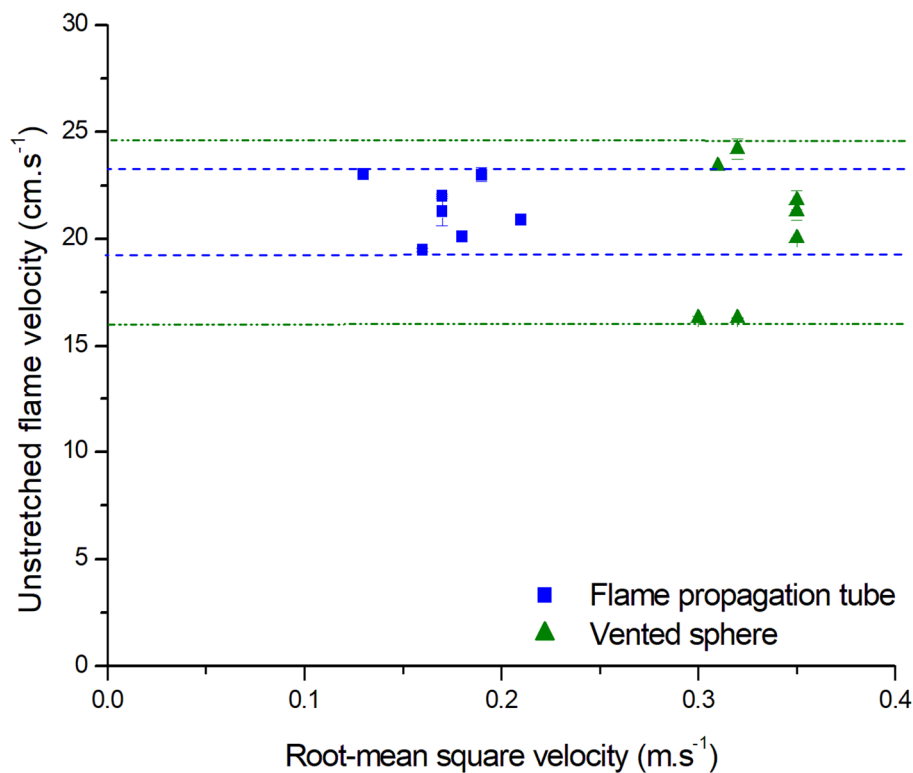
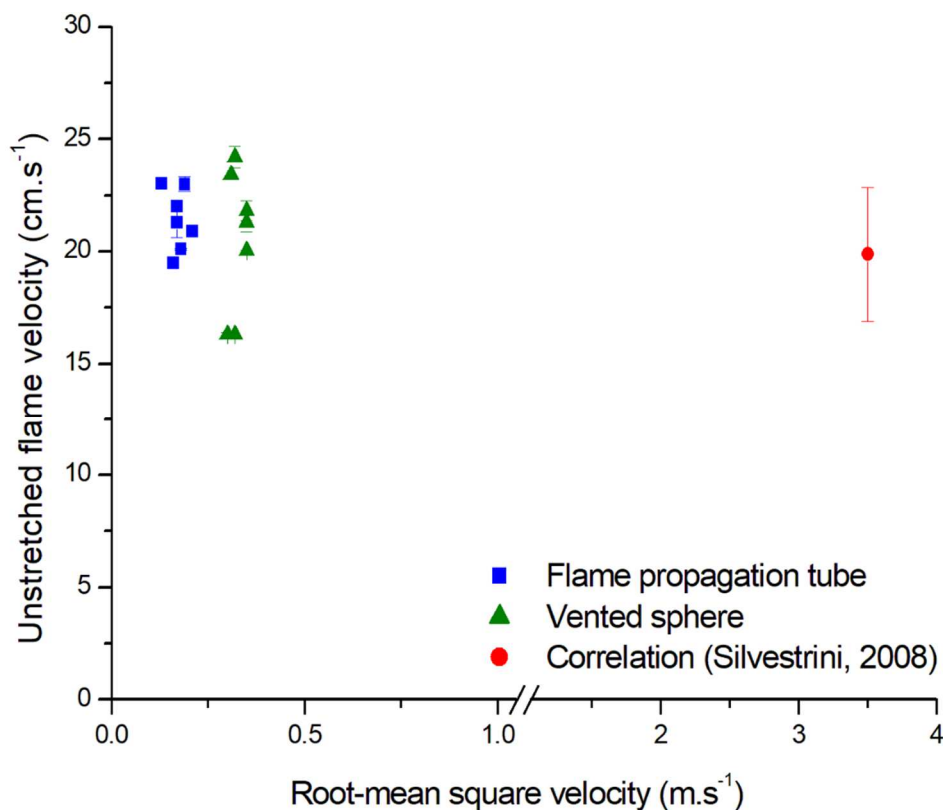


Figure 13. Evolution of the unstretched burning velocity with the root mean square velocity in the flame propagation tube and in the open 20L sphere

514 The values of the unstretched burning velocities obtained through visualization of the flame  
 515 propagation were then compared to the value acquired by pressure-time recording in the  
 516 standard 20L apparatus (Figure 14). Using the semi-empirical correlation previously detailed  
 517 (Equation 7), an unstretched burning velocity of  $19.9 \text{ cm.s}^{-1}$  is obtained at a root mean square  
 518 velocity of  $3.5 \text{ m.s}^{-1}$  while the same value was reached in the flame propagation tube and  
 519 vented 20L sphere for root mean square velocities of  $0.2 \text{ m.s}^{-1}$  and  $0.3 \text{ m.s}^{-1}$  respectively. This  
 520 is due to the fact that the empirical coefficient of the correlation was established by  
 521 considering explosion tests performed in standard conditions in the 20L sphere. The equation  
 522 was applied with a coefficient 0.11 as proposed by the authors, but it makes it valid only for  
 523  $(dP/dt)_m$  and  $P_m$  obtained with an ignition delay time of 60 ms, i.e. a root-mean square  
 524 velocity of  $3.5 \text{ m.s}^{-1}$ , as previously presented in Table 1.



525  
 526 *Figure 14. Evolution of the unstretched burning velocity with the root mean square velocity*  
 527 *measured in the flame propagation tube, the vented 20L sphere and the standard 20L sphere*

528

529 The laminar burning velocity was then calculated by application of Silvestrini's correlation  
 530 (eq. 6) to the parameters  $P_m$  and  $(dP/dt)_m$  obtained with a standard explosion in the 20L  
 531 sphere, with an ignition energy of 10J and ignition delay time of 60 ms. Moreover, since  
 532 Cuervo (2015) and Dahoe et al. (2001) showed that the vertical velocity of the particles is  
 533 close to zero for ignition delay times greater than 300 ms in the propagation tube and in the  
 534 20L sphere, and since the flame kernel stays put when growing, the flame propagation  
 535 visualized in both equipment is considered to be independent of the turbulence level, and the  
 536 laminar burning velocity was then estimated by averaging the measured values of unstretched  
 537 burning velocities. However, in addition to the difficulties to identify the flame kernel in the  
 538 vented sphere, significant fluctuations in the velocity in the sphere can explain the more  
 539 important scattering of the values of the unstretched burning velocities obtained compared to  
 540 the ones obtained in the tube. The values of laminar burning velocity of the nanocellulose  
 541 determined for each method are presented in Table 2.

542

543 *Table 2. Laminar burning velocity of the nanocellulose estimated by the three different*  
 544 *methods*

<i>Method</i>	<i>Flame propagation tube (flame visualization)</i>	<i>Open 20L sphere (flame visualization)</i>	<i>Standard 20L sphere (pressure evolution)</i>
<i>Laminar burning velocity (<math>cm.s^{-1}</math>)</i>	$21.4 \pm 1.4$	$20.5 \pm 3.2$	$19.9 \pm 3.0$

545

546

547 It first appears that the three methods lead to similar results, the propagation tube providing  
 548 the less scattered values of laminar burning velocity. The calculation performed using  
 549 Silvestrini et al. (2008) correlation also provides a value in good agreement with the values  
 550 measured by flame propagation analysis, but with a higher uncertainty than in the propagation

tube. It is mainly due to the lack of reproducibility of the experiments in the standard 20L sphere at 60 ms (Proust et al., 2007). Indeed, at an ignition delay time of 60 ms, the turbulence level is in the “transition stage” identified by Murillo et al. (2018), and turbulence variations have a strong impact on the maximum rate of pressure rise. Adapting the correlation with a coefficient estimated from experiments performed in pseudo-laminar conditions, i.e. higher ignition delay time, would then improve the accuracy of the estimation of the laminar burning velocity. It would then be interesting to use flame propagation analysis on different powders to determine such a coefficient and to apply it to the correlation established by Silvestrini et al. (2008). However, this adapted correlation would have to be used with  $P_m$  and  $(dP/dt)_m$  measured in the same turbulent conditions than the coefficient, which can limit the application of such a relation. To apply this correlation to different conditions and represent industrial situations, an evaluation of the evolution of the correlation coefficient with the initial turbulence is then required.

Since the correlation has been validated for nanocellulose at 60 ms, a first estimation of the coefficient dependency with the turbulence was realized through explosion tests conducted in the standard closed 20L vessel by varying the ignition delay time from 60 ms to 300 ms. By applying the correlation used previously and considering the value obtained at 60 ms as a reference, the corrected correlation coefficients were estimated for different root-mean square velocities, as presented in Figure 15. It appears that the value to consider to obtain the laminar burning velocity of  $19.9 \text{ cm.s}^{-1}$  increases when decreasing the root-mean square velocity, reaching 0.28 at  $0.4 \text{ m.s}^{-1}$ , i.e. more than twice the initial value of 0.11 at  $3.5 \text{ m.s}^{-1}$ . The correlation coefficient follows the same evolution as the time after dispersion with the root-mean square velocity, which implies that it could be correlated by a decay law similar to the one established by Dahoe et al. (2001) relating the root-mean square velocity and the time. The determination of such a relation, coupled with a correlation linking the evolution of

(dP/dt)<sub>m</sub> with the initial turbulence, could then enable an accurate determination of the laminar burning velocity in the closed 20L sphere.

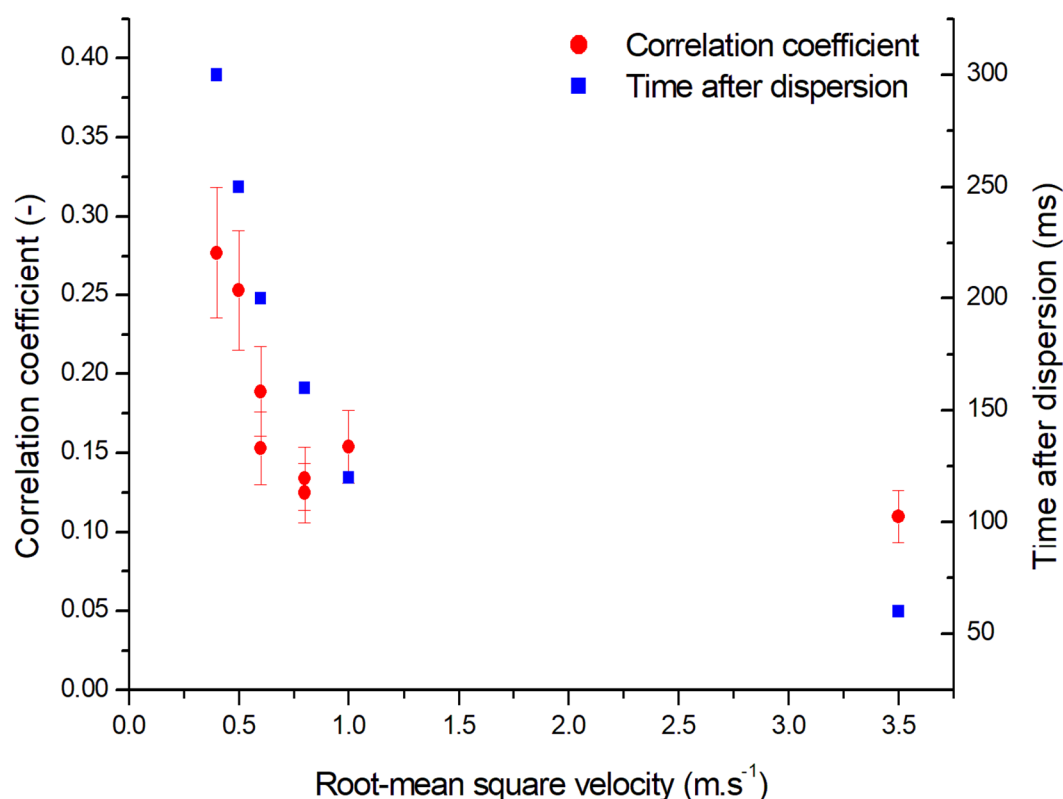


Figure 15. Evolution of the time after dispersion and the coefficient from Silvestrini's correlation with the root-mean square velocity in the 20L sphere

Krause and Kasch (2000) reported laminar burning velocities presented in the literature for different concentrations of two organic powders: lycopodium and cornstarch. Values from 17 cm.s<sup>-1</sup> to 69 cm.s<sup>-1</sup> were then obtained for lycopodium, and velocities between 13 cm.s<sup>-1</sup> and 59 cm.s<sup>-1</sup> were acquired for cornstarch. More specifically, van der Wel (1993) reported a laminar flame velocity for cornstarch of 13 cm.s<sup>-1</sup> at 400 g.m<sup>-3</sup> using the 20L sphere coupled with a correlation based on Mallard and Le Chatelier thermal theory, and 13 to 20 cm.s<sup>-1</sup> using the burner method for concentrations from 400 g.m<sup>-3</sup> to 600 g.m<sup>-3</sup>. Haghir and Bidabadi (2010) also calculated laminar burning velocities for organic powders from 15 cm.s<sup>-1</sup> to 45

cm.s<sup>-1</sup> for concentrations from 30 g.m<sup>-3</sup> to 100 g.m<sup>-3</sup> using a model considering the thermal radiation effect. Moreover, Cuervo et al. (2017) also measured a laminar burning velocity for 915 g.m<sup>-3</sup> of starch around 19.9 cm.s<sup>-1</sup>. Since starch and nanocellulose have similar structures and composition, these values are in good agreement with the value of 21.4 cm.s<sup>-1</sup> obtained in the tube for the nanocellulose, despite the different concentrations.

The Markstein length was also calculated from video analysis of the flame propagations in the tube and the vented sphere. Similar values were obtained in both equipment, with a mean value of -0.25 mm in the propagation tube and -0.19 mm in the vented sphere. A negative value of the Markstein length means that the flame speed increases with the stretch rate, implying that the flame is unstable. However, the obtained values are very low (absolute values usually lower than 1 mm), and some positive values up to 0.3 mm were also obtained when analyzing the flame propagation videos under certain conditions, which makes it difficult to draw an accurate conclusion on the Markstein length of nanocellulose flames. Nevertheless, it should be stressed that these values are much lower than that obtained by Dahoe et al. (2002) for cornstarch-air mixtures, i.e. 11.0 mm, but are a bit higher than those encountered for methane-air mixtures, i.e. from 0.1 to 0.2 mm. This can be related to the fact that nanocellulose is prone to devolatilization when exposed to high temperatures.

### 3.5. Influence of the dust concentration

Even though the theoretical stoichiometric concentration for the combustion of nanocellulose is of approximately 250 g.m<sup>-3</sup>, it appears in Figure 8 that the most severe explosions were obtained for concentrations of 750 g.m<sup>-3</sup> and 1000 g.m<sup>-3</sup> in terms of maximum overpressure and maximum rate of pressure rise. It is then legitimate to investigate the influence of the dust concentration on the laminar burning velocity. However, the estimation of the flame propagation at high concentration is difficult since the dust cloud can hinder the visualization of the flame kernel. A few tests were performed in the flame propagation tube at larger dust



concentrations (i.e.  $750 \text{ g.m}^{-3}$ ) and a slight increase of the flame velocity was observed. However, since it is currently impossible to accurately estimate the laminar burning velocity at high concentration using the flame propagation visualization method due to flame obscuring, it was calculated as previously, using the correlation established by Silvestrini et al. (2008) coupled with the standard results presented in Figure 8. It has to be noticed that those experiments were carried out with chemical ignitors of 10 kJ, contrary to the results presented in Figure 14 carried out using an electrical spark of 10 J, which limits the impact of the shock wave created by the igniters.

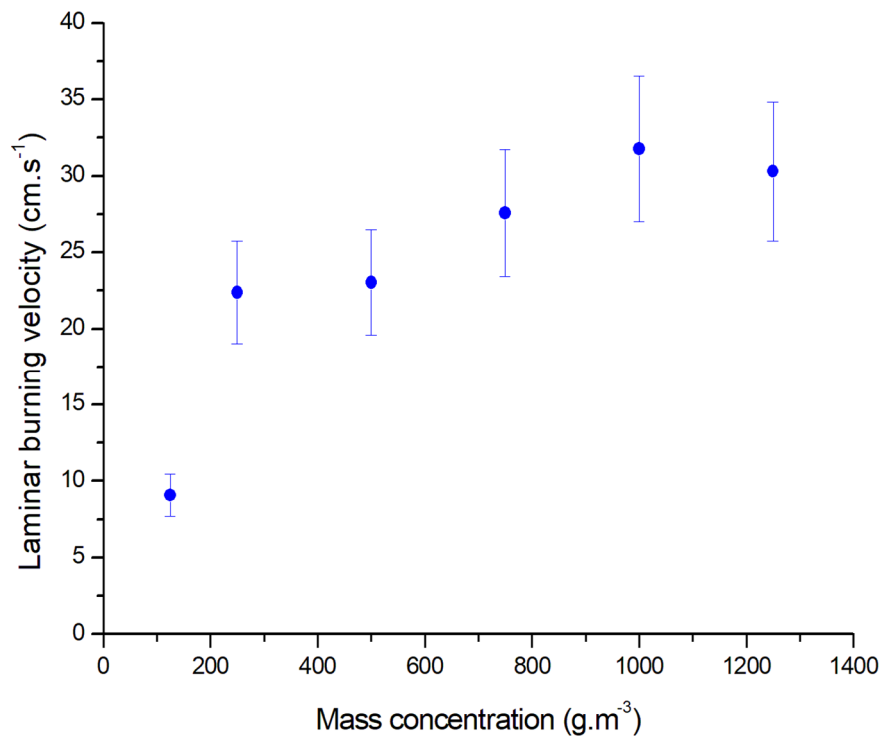


*Figure 16. Evolution of the laminar burning velocity calculated by a semi-empiric correlation with the mass concentration*

Since the laminar burning velocity is calculated from the knowledge of the maximum overpressure and the maximum rate of pressure rise, it follows the same evolution as those parameters (Figure 16). The maximum value is obtained around  $32 \text{ cm.s}^{-1}$  for a concentration of  $1000 \text{ g.m}^{-3}$ . This value is close to the laminar burning velocity of stoichiometric methane

generally reported to be around  $35 \text{ cm.s}^{-1}$  (Bradley et al., 2017) for a maximum overpressure of 7.2 bars and a  $K_g$  of  $395 \text{ bar.m.s}^{-1}$ , measured in standard conditions by Torrado et al. (2017a). The value calculated for the nanocellulose with the correlation then seems higher than expected considering its medium explosion severity compared to pure methane, thus questioning the validity of the correlation for high concentrations. Indeed, Silvestrini et al. (2008) have chosen 24 dust-air mixtures to calculate the coefficient for the semi-empiric correlation. However, it should be stressed that, among these mixtures, only 3 dust concentrations were higher than  $500 \text{ g.m}^{-3}$ . The same method considering mixtures with a larger range of concentrations may then extend the validity of the correlation to higher concentrations. Indeed, in order to realize an accurate evaluation of the explosion consequences, the influence of the dust concentration on the laminar burning velocity must be considered. The value corresponding to the worst-case scenario could then be loaded in simulation and by adding the contribution of the turbulence of the dust cloud, the consequences of an explosion in specific conditions can be estimated. It implies that the turbulent burning velocity has to be deduced from the knowledge of the laminar burning velocity and the turbulence level.

### 3.6. Application of turbulent burning velocity models

Several correlations relating the turbulent burning velocity to the laminar burning velocity and the turbulence intensity exist in the literature, and were notably summarized by Andrews et al. (1975), Dahoe et al. (2013) and Gülder (1991). Although these models were established for premixed flames, some of the correlations presented by Dahoe et al. (2013) were tested in this study to be compared, in a reverse approach, to the values of turbulent burning velocities obtained by analyzing the flame propagation in the tube (Table 3). In addition to those correlations, the relation established by Popat et al. (1996) used in the FLACS-DustEx CFD

code (relation (g)) was applied to the experimental data produced in this work (Ghaffari et al., 2019; Skjold, 2007).

*Table 3. Some turbulent burning velocity models for premixed flame propagation*

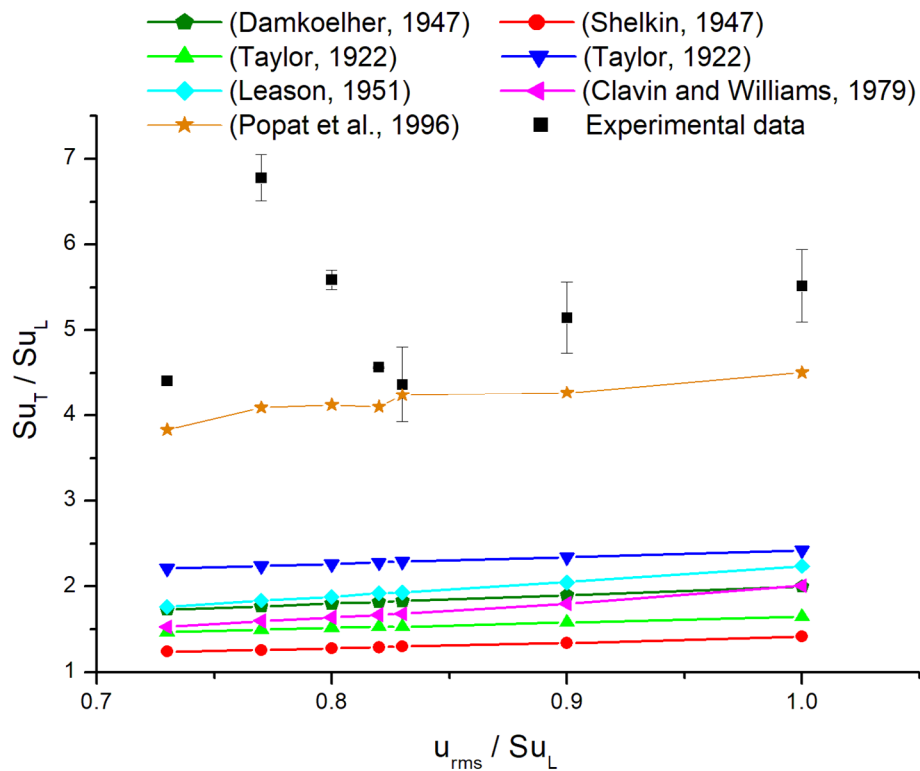
Notation	Formula	Reference
(a)	$\frac{Su_T}{Su_L} = 1 + \frac{u_{rms}}{Su_L}$	(Damkoehler, 1947)
(b)	$\frac{Su_T}{Su_L} = \sqrt{1 + \left(\frac{u_{rms}}{Su_L}\right)^2}$	(Shelkin, 1947)
(c)	$\frac{Su_T}{Su_L} = 1 + \sqrt{\frac{5}{12} \frac{u_{rms}}{Su_L}}$	(Taylor, 1922)
(d)	$\frac{Su_T}{Su_L} = 1 + \sqrt{2} \left(\frac{u_{rms}}{Su_L}\right)^{1/2}$	(Taylor, 1922)
(e)	$\frac{Su_T}{Su_L} = \sqrt{1 + \left(\frac{2 u_{rms}}{Su_L}\right)^2}$	(Leason, 1951)
(f)	$\frac{Su_T}{Su_L} = 1 + \left(\frac{u_{rms}}{Su_L}\right)^2$	(Clavin and Williams, 1979)
(g)	$Su_T = 15.1 Su_L^{0.784} u_{rms}^{0.412} l_i^{0.196}$	(Popat et al., 1996)

Concerning the models mentioned by Dahoe et al. (2013), it appears in Figure 17 that an average difference of 55% is observed between the model providing the best fitting, i.e. model (d) from Taylor (1922), and experimental data, meaning none of the models actually fits the experimental data. This statement is not only related to the fact that correlations established for premixed flame were applied to a diffusional flame, since it was previously underlined for premixed flames of methane-air and hydrogen-air mixtures by Dahoe et al. (2013), who then proposed a semi-empiric correlation of the following form :

$$\frac{Su_T}{Su_L} = 1 + a_1 D_a^{a_2} \left(\frac{u_{rms}}{Su_L}\right)^{a_3} \quad (8)$$

667  $a_1$ ,  $a_2$  and  $a_3$  being three coefficients to determine experimentally and  $Da$  the Damköhler  
 668 number. They observed that two distinct sets of coefficients exist in their operating  
 669 conditions, revealing that the establishment of a unique correlation allowing the calculation of  
 670 the turbulent burning velocity from the knowledge of the laminar burning velocity and the  
 671 turbulence intensity is not trivial, even for gases.

672 The model established by Popat et al. (1996) and considered in the CFD code used by Skjold  
 673 (2007) clearly provides the best fitting with the experimental data from this work, with an  
 674 average difference of 20%. The difference can be due to experimental uncertainties, notably  
 675 concerning the point at  $Su_T/Su_L = 6.8$ , but also to the different assumptions concerning the  
 676 correlation, such as a constant kinematic viscosity and the integral length scale  $l_i$  equal to 1  
 677 cm (Skjold, 2003). A proper estimation of the turbulent velocity being essential to provide an  
 678 accurate risk assessment concerning the consequences of an explosion, further investigations  
 679 on such models is required.



680

*Figure 17. Comparison between models listed in Table 3 and experimental turbulent burning velocities measured in the flame propagation tube*

#### **4. Conclusion**

The laminar burning velocity of nanocellulose has been assessed by three different methods including the direct visualization of the flame propagation in a vertical 1 m long tube or in a vented 20L sphere coupled with the application of relationships relating the flame speed and its stretching, and the use of correlations based on the pressure time evolution during a standard explosion test. Both visualization methods, tube or open sphere, lead to similar results, consistent with the values previously presented in the literature for other organic powders, validating this experimental approach for organic powders. Moreover, these results were compared with those obtained from standard tests in the 20L sphere using a semi-empiric correlation relating the pressure evolution and the flame velocity. All three methods lead to similar values of nanocellulose-air laminar burning velocity, i.e. approximately 21 cm.s<sup>-1</sup>.

The use of nanopowders for such analyses allows reaching very low turbulence levels and thus reduces the impact of turbulence on the flame kernel growth, approaching ‘pseudo-laminar’ conditions. It has notably been underlined that using such flame propagation analyses at low turbulence can support the development of semi-empiric correlations allowing the estimation of the laminar burning velocity from the knowledge of the pressure-time evolution in the standard 20L sphere. The laminar flame velocity being an intrinsic property of the dust-air mixture, it is likely that such techniques could be used in addition to standardized tests in the 20L sphere in order to increase the scope of their results. Indeed, results obtained from standard tests in standards equipment can only be applied to larger enclosures if reliable scaling laws are available. Otherwise, these results are only valid for the

specific operating conditions defined by the standards. But, as previously stated in introduction, the validity of the widespread ‘cube-root-law’ depends on several limiting assumptions. Therefore, the determination of a laminar burning velocity can help to overcome such limitations by providing an accurate risk assessment independent from the operating conditions.

However, the knowledge of the laminar burning velocity of a mixture is valuable for industrial purposes only if reliable models exist, converting it to a spatial/turbulent burning velocity knowing the turbulent conditions of the cloud. This point is far from being trivial for dusts and some efforts still have to be made in this direction.

## Acknowledgments

The authors would like to warmly acknowledge Claire Dazon, Sébastien Bau and Olivier Witschger (INRS – Vandoeuvre-les-Nancy, France) for FMPS measurements and rotative drum tests. They also would like to thank Augustin Charvet (LRGP CNRS-UL) for SMPS measurements as well as David Brunello, Charly Koenig and Christian Blanchard (LRGP CNRS-UL) for their invaluable contributions in experimental setup design. This work was supported financially by the French Ministry for the Ecological and Solidary Transition and The French Ministry for Higher Education and Research.

## References

- Abitbol, T., Rivkin, A., Cao, Y., Nevo, Y., Abraham, E., Ben-Shalom, T., Lapidot, S., Shoseyov, O., 2016. Nanocellulose, a tiny fiber with huge applications. *Current Opinion in Biotechnology, Systems biology - Nanobiotechnology* 39, 76–88.  
<https://doi.org/10.1016/j.copbio.2016.01.002>

730 Amyotte, P.R., 2014. Some myths and realities about dust explosions. *Process Safety and*  
 731 *Environmental Protection, Loss Prevention* 2013 92, 292–299.  
 732 <https://doi.org/10.1016/j.psep.2014.02.013>

733 Amyotte, P.R., Chippett, S., Pegg, M.J., 1988. Effects of turbulence on dust explosions.  
 734 *Progress in Energy and Combustion Science* 14, 293–310.  
 735 [https://doi.org/10.1016/0360-1285\(88\)90016-0](https://doi.org/10.1016/0360-1285(88)90016-0)

736 Andrews, G.E., Bradley, D., 1972. Determination of burning velocities: A critical review.  
 737 *Combustion and Flame* 18, 133–153. [https://doi.org/10.1016/S0010-2180\(72\)80234-7](https://doi.org/10.1016/S0010-2180(72)80234-7)

738 Andrews, G.E., Bradley, D., Lwakabamba, S.B., 1975. Turbulence and turbulent flame  
 739 propagation—A critical appraisal. *Combustion and Flame* 24, 285–304.  
 740 [https://doi.org/10.1016/0010-2180\(75\)90163-7](https://doi.org/10.1016/0010-2180(75)90163-7)

741 Bartknecht, W., 1989. Dust-explosions: course, prevention, protection. Springer-Verlag.

742 Belerrajoul, M., 2019. Modélisation multi-échelle de la combustion d'un nuage de particules  
 743 (PhD Thesis). National Polytechnic Institute of Toulouse.

744 Bidabadi, M., Azad, A.V., 2015. Effects of radiation on propagating spherical flames of dust–  
 745 air mixtures. *Powder Technology* 276, 45–59.  
 746 <https://doi.org/10.1016/j.powtec.2014.12.044>

747 Boilard, S.P., Amyotte, P.R., Khan, F.I., Dastidar, A.G., Eckhoff, R.K., 2013. Explosibility of  
 748 micron- and nano-size titanium powders. *Journal of Loss Prevention in the Process*  
 749 *Industries* 26, 1646–1654. <https://doi.org/10.1016/j.jlp.2013.06.003>

750 Bouillard, J., Vignes, A., Dufaud, O., Perrin, L., Thomas, D., 2010. Ignition and explosion  
 751 risks of nanopowders. *Journal of Hazardous Materials* 181, 873–880.  
 752 <https://doi.org/10.1016/j.jhazmat.2010.05.094>

753 Bradley, D., 2000. Flame Propagation in a Tube: The Legacy of Henri Guenoeche.  
 754 Combustion Science and Technology 158, 15–33.  
 755 <https://doi.org/10.1080/00102200008947325>

756 Bradley, D., Chen, Z., Swithenbank, J.R., 1989. Burning rates in turbulent fine dust-air  
 757 explosions. Symposium (International) on Combustion 22, 1767–1775.  
 758 [https://doi.org/10.1016/S0082-0784\(89\)80190-0](https://doi.org/10.1016/S0082-0784(89)80190-0)

759 Bradley, D., Lawes, M., Mumby, R., 2017. Burning velocity and Markstein length blending  
 760 laws for methane/air and hydrogen/air blends. Fuel 187, 268–275.  
 761 <https://doi.org/10.1016/j.fuel.2016.09.032>

762 Bradley, D., Lee, J.H., 1984. . Proceedings of the first international colloquium on the  
 763 explosibility of industrial dusts 220–223.

764 CelluForce, 2016, Product specification of CelluForce NCV100, CelluForce company,  
 765 Montreal, Canada.

766 Chen, Z., Ju, Y., 2007. Theoretical analysis of the evolution from ignition kernel to flame ball  
 767 and planar flame. Combustion Theory and Modelling 11, 427–453.  
 768 <https://doi.org/10.1080/13647830600999850>

769 Clavin, P., 1985. Dynamic behavior of premixed flame fronts in laminar and turbulent flows.  
 770 Progress in Energy and Combustion Science 11, 1–59. [https://doi.org/10.1016/0360-](https://doi.org/10.1016/0360-1285(85)90012-7)  
 771 [1285\(85\)90012-7](https://doi.org/10.1016/0360-1285(85)90012-7)

772 Clavin, P., Williams, F.A., 1979. Theory of premixed-flame propagation in large-scale  
 773 turbulence. Journal of Fluid Mechanics 90, 589–604.  
 774 <https://doi.org/10.1017/S002211207900241X>

775 Clouthier, M.P., Taveau, J.R., Dastidar, A.G., Morrison, L.S., Zalosh, R.G., Ripley, R.C.,  
 776 Khan, F.I., Amyotte, P.R., 2019. Iron and aluminum powder explosibility in 20-L and



777 1- m 3 chambers. *Journal of Loss Prevention in the Process Industries* 62, 103927.  
 778 <https://doi.org/10.1016/j.jlp.2019.103927>

779 Cuervo, N., 2015. Influences of turbulence and combustion regimes on explosions of gas-dust  
 780 hybrid mixtures (PhD Thesis). The University of Lorraine, France.

781 Cuervo, N., Dufaud, O., Perrin, L., 2017. Determination of the burning velocity of gas/dust  
 782 hybrid mixtures. *Process Safety and Environmental Protection* 109, 704–715.  
 783 <https://doi.org/10.1016/j.psep.2017.06.009>

784 Dahoe, A.E., Cant, R.S., Pegg, M.J., Scarlett, B., 2001. On the transient flow in the 20-liter  
 785 explosion sphere. *Journal of Loss Prevention in the Process Industries* 14, 475–487.  
 786 [https://doi.org/10.1016/S0950-4230\(01\)00052-3](https://doi.org/10.1016/S0950-4230(01)00052-3)

787 Dahoe, A.E., Hanjalic, K., Scarlett, B., 2002a. Determination of the laminar burning velocity  
 788 and the Markstein length of powder–air flames. *Powder Technology*, Special issue i in  
 789 Honour of Prof Jimbo 122, 222–238. [https://doi.org/10.1016/S0032-5910\(01\)00419-3](https://doi.org/10.1016/S0032-5910(01)00419-3)

790 Dahoe, A.E., Hanjalic, K., Scarlett, B., 2002b. Determination of the laminar burning velocity  
 791 and the Markstein length of powder–air flames. *Powder Technology*, Special issue i in  
 792 Honour of Prof Jimbo 122, 222–238. [https://doi.org/10.1016/S0032-5910\(01\)00419-3](https://doi.org/10.1016/S0032-5910(01)00419-3)

793 Dahoe, A.E., Skjold, T., Roekaerts, D.J.E.M., Pasman, H.J., Eckhoff, R.K., Hanjalic, K.,  
 794 Donze, M., 2013. On the Application of the Levenberg–Marquardt Method in  
 795 Conjunction with an Explicit Runge–Kutta and an Implicit Rosenbrock Method to  
 796 Assess Burning Velocities from Confined Deflagrations. *Flow, Turbulence and*  
 797 *Combustion* 91, 281–317. <https://doi.org/10.1007/s10494-013-9462-z>

798 Dahoe, A.E., Zevenbergen, J.F., Lemkowitz, S.M., Scarlett, B., 1996. Dust explosions in  
 799 spherical vessels: The role of flame thickness in the validity of the ‘cube-root law.’

Journal of Loss Prevention in the Process Industries 9, 33–44.  
[https://doi.org/10.1016/0950-4230\(95\)00054-2](https://doi.org/10.1016/0950-4230(95)00054-2)

Damkoehler, G., 1947. The Effect of Turbulence on the Flame Velocity in Gas Mixtures.

Di Benedetto, A., Garcia-Agreda, A., Dufaud, O., Khalili, I., Sanchirico, R., Perrin, L., Russo, P., 2011. Flame propagation of dust and gas-air mixtures in a tube. Proceedings of the 7th Mediterranean Combustion Symposium 12.

Di Benedetto, A., Russo, P., 2007. Thermo-kinetic modelling of dust explosions. Journal of Loss Prevention in the Process Industries, Selected Papers Presented at the Sixth International Symposium on Hazards, Prevention and Mitigation of Industrial Explosions 20, 303–309. <https://doi.org/10.1016/j.jlp.2007.04.001>

Di Benedetto, Russo, P., Sanchirico, R., Sarli, V.D., 2013. CFD simulations of turbulent fluid flow and dust dispersion in the 20 liter explosion vessel. AIChE Journal 59, 2485–2496. <https://doi.org/10.1002/aic.14029>

Dufaud, O., Vignes, A., Henry, F., Perrin, L., Bouillard, J., 2011. Ignition and explosion of nanopowders: something new under the dust. Journal of Physics: Conference Series 304, 012076. <https://doi.org/10.1088/1742-6596/304/1/012076>

Eckhoff, R.K., 2012. Does the dust explosion risk increase when moving from  $\mu\text{m}$ -particle powders to powders of nm-particles? Journal of Loss Prevention in the Process Industries 25, 448–459. <https://doi.org/10.1016/j.jlp.2011.11.011>

Eckhoff, R.K., 2003. Dust Explosions in the Process Industries - 3rd Edition, 3rd ed. Gulf Professional Publishing.

EN 14034-1, 2004. Determination of explosion characteristics of dust clouds — Part 1: Determination of the maximum explosion pressure  $P_{\text{max}}$  of dust clouds.

823 EN 14034-2, 2006. Determination of explosion characteristics of dust clouds — Part 2:  
 824 Determination of the maximum rate of explosion pressure rise (dp/dt)<sub>max</sub> of dust  
 825 clouds.

826 Frankel, M.L., Sivashinsky, G.I., 1984. On Quenching of Curved Flames. Combustion  
 827 Science and Technology 40, 257–268. <https://doi.org/10.1080/00102208408923809>

828 Ghaffari, M., Hoffmann, A.C., Skjold, T., Eckhoff, R.K., van Wingerden, K., 2019. A brief  
 829 review on the effect of particle size on the laminar burning velocity of flammable dust:  
 830 Application in a CFD tool for industrial applications. Journal of Loss Prevention in the  
 831 Process Industries 62, 103929. <https://doi.org/10.1016/j.jlp.2019.103929>

832 Going, J.E., Chatrathi, K., Cashdollar, K.L., 2000. Flammability limit measurements for dusts  
 833 in 20-L and 1-m<sup>3</sup> vessels. Journal of Loss Prevention in the Process Industries 13,  
 834 209–219. [https://doi.org/10.1016/S0950-4230\(99\)00043-1](https://doi.org/10.1016/S0950-4230(99)00043-1)

835 Goroshin, S., Tang, F.-D., Higgins, A.J., Lee, J.H., 2011. Laminar dust flames in a reduced-  
 836 gravity environment. Acta Astronautica 68, 656–666.  
 837 <https://doi.org/10.1016/j.actaastro.2010.08.038>

838 Gülder, Ö.L., 1991. Turbulent premixed flame propagation models for different combustion  
 839 regimes. Symposium (International) on Combustion, Twenty-Third Symposium  
 840 (International) on Combustion 23, 743–750. [https://doi.org/10.1016/S0082-](https://doi.org/10.1016/S0082-0784(06)80325-5)  
 841 [0784\(06\)80325-5](https://doi.org/10.1016/S0082-0784(06)80325-5)

842 Haghiri, A., Bidabadi, M., 2010. Modeling of laminar flame propagation through organic dust  
 843 cloud with thermal radiation effect. International Journal of Thermal Sciences 49,  
 844 1446–1456. <https://doi.org/10.1016/j.ijthermalsci.2010.03.013>

845 Harris, R.J., 1983. The investigation and control of gas explosions in buildings and heating  
 846 plant. E. & F.N. Spon in association with the British Gas Corp.

847 Jespen, T., 2016. ATEX—Explosive Atmospheres, Springer Series in Reliability Engineering.  
848 Springer International Publishing, Cham. <https://doi.org/10.1007/978-3-319-31367-2>

849 Joulin, G., Clavin, P., 1979. Linear stability analysis of nonadiabatic flames: Diffusional-  
850 thermal model. *Combustion and Flame* 35, 139–153. [https://doi.org/10.1016/0010-](https://doi.org/10.1016/0010-2180(79)90018-X)  
851 [2180\(79\)90018-X](https://doi.org/10.1016/0010-2180(79)90018-X)

852 Julien, P., Whiteley, S., Soo, M., Goroshin, S., Frost, D.L., Bergthorson, J.M., 2017. Flame  
853 speed measurements in aluminum suspensions using a counterflow burner.  
854 *Proceedings of the Combustion Institute* 36, 2291–2298.  
855 <https://doi.org/10.1016/j.proci.2016.06.150>

856 Karlovitz, B., Denniston, D.W., Wells, F.E., 1951. Investigation of Turbulent Flames. *J.*  
857 *Chem. Phys.* 19, 541–547. <https://doi.org/10.1063/1.1748289>

858 Kosinski, P., Nyheim, R., Asokan, V., Skjold, T., 2013. Explosions of carbon black and  
859 propane hybrid mixtures. *Journal of Loss Prevention in the Process Industries* 26, 45–  
860 51. <https://doi.org/10.1016/j.jlp.2012.09.004>

861 Krause, U., Kasch, T., 2000. The influence of flow and turbulence on flame propagation  
862 through dust-air mixtures. *Journal of Loss Prevention in the Process Industries* 13,  
863 291–298. [https://doi.org/10.1016/S0950-4230\(99\)00062-5](https://doi.org/10.1016/S0950-4230(99)00062-5)

864 Krietsch, A., Scheid, M., Schmidt, M., Krause, U., 2015. Explosion behaviour of metallic  
865 nano powders. *Journal of Loss Prevention in the Process Industries* 36, 237–243.  
866 <https://doi.org/10.1016/j.jlp.2015.03.016>

867 Law, C.K., 2006. *Combustion Physics* by Chung K. Law [WWW Document]. Cambridge  
868 Core. <https://doi.org/10.1017/CBO9780511754517>

869 Leason, D.B., 1951. Turbulence and flame propagation in premixed gases. *Fuel* 30, 233–239.

870 Lee, J., Peraldi, O., Knystautas, R., 1993. Microgravity combustion of dust suspension, in:  
 871 31st Aerospace Sciences Meeting. Presented at the 31st Aerospace Sciences Meeting,  
 872 American Institute of Aeronautics and Astronautics, Reno,NV,U.S.A.  
 873 <https://doi.org/10.2514/6.1993-714>

874 Lewis, B., von Elbe, G., 1987. Combustion, Flames and Explosions of Gases. Elsevier.  
 875 <https://doi.org/10.1016/C2009-0-21751-X>

876 Lomba, R., Laboureur, P., Dumand, C., Chauveau, C., Halter, F., 2019. Determination of  
 877 aluminum-air burning velocities using PIV and Laser sheet tomography. Proceedings  
 878 of the Combustion Institute 37, 3143–3150.  
 879 <https://doi.org/10.1016/j.proci.2018.07.013>

880 Markstein, G.H., 1964. Non-steady flame Propagation. P22, Pergarmon, New York.

881 Mazumdar, A., 2013. Principles and Techniques of Schlieren Imaging Systems.  
 882 <https://doi.org/10.7916/D8TX3PWV>

883 McBride, B.J., Gordon, S., 1996. Computer Program for Calculation of Complex Chemical  
 884 Equilibrium Compositions and Applications II. Users Manual and Program  
 885 Description. NASA. RP 1311.

886 Miao, J., Leung, C.W., Huang, Z., Cheung, C.S., Yu, H., Xie, Y., 2014. Laminar burning  
 887 velocities, Markstein lengths, and flame thickness of liquefied petroleum gas with  
 888 hydrogen enrichment. International Journal of Hydrogen Energy 39, 13020–13030.  
 889 <https://doi.org/10.1016/j.ijhydene.2014.06.087>

890 Mittal, M., 2014. Explosion characteristics of micron- and nano-size magnesium powders.  
 891 Journal of Loss Prevention in the Process Industries 27, 55–64.  
 892 <https://doi.org/10.1016/j.jlp.2013.11.001>

893 Mohan, S., Ermoline, A., Dreizin, E.L., 2012. Pyrophoricity of nano-sized aluminum  
 894 particles. *J Nanopart Res* 14, 723. <https://doi.org/10.1007/s11051-012-0723-x>

895 Murillo, C., 2016. Experimental and numerical approaches to particles dispersion in a  
 896 turbulent flow : application to dust explosions (PhD Thesis). Université de Lorraine,  
 897 France.

898 Murillo, C., Amín, M., Bardin-Monnier, N., Muñoz, F., Pinilla, A., Ratkovich, N., Torrado,  
 899 D., Vizcaya, D., Dufaud, O., 2018. Proposal of a new injection nozzle to improve the  
 900 experimental reproducibility of dust explosion tests. *Powder Technology* 328, 54–74.  
 901 <https://doi.org/10.1016/j.powtec.2017.12.096>

902 Popat, N.R., Catlin, C.A., Arntzen, B.J., Lindstedt, R.P., Hjertager, B.H., Solberg, T., Saeter,  
 903 O., Van den Berg, A.C., 1996. Investigations to improve and assess the accuracy of  
 904 computational fluid dynamic based explosion models. *Journal of Hazardous Materials*  
 905 45, 1–25. [https://doi.org/10.1016/0304-3894\(95\)00042-9](https://doi.org/10.1016/0304-3894(95)00042-9)

906 Proust, C., 2006. Flame propagation and combustion in some dust-air mixtures. *Journal of*  
 907 *Loss Prevention in the Process Industries* 19, 89–100.  
 908 <https://doi.org/10.1016/j.jlp.2005.06.026>

909 Proust, C., Accorsi, A., Dupont, L., 2007. Measuring the violence of dust explosions with the  
 910 “20l sphere” and with the standard “ISO 1m3 vessel”: Systematic comparison and  
 911 analysis of the discrepancies. *Journal of Loss Prevention in the Process Industries*,  
 912 *Selected Papers Presented at the Sixth International Symposium on Hazards,*  
 913 *Prevention and Mitigation of Industrial Explosions* 20, 599–606.  
 914 <https://doi.org/10.1016/j.jlp.2007.04.032>

915 Pu, Y., Podfilipski, J., Jarosiński, J., 1998. Constant Volume Combustion of Aluminum and  
 916 Cornstarch Dust in Microgravity. *Combustion Science and Technology* 135, 255–267.  
 917 <https://doi.org/10.1080/00102209808924160>

918 Pu, Y.K., Jarosinski, J., Johnson, V.G., Kauffman, C.W., 1991. Turbulence effects on dust  
 919 explosions in the 20-liter spherical vessel. *Symposium (International) on Combustion*,  
 920 Twenty-Third Symposium (International) on Combustion 23, 843–849.  
 921 [https://doi.org/10.1016/S0082-0784\(06\)80338-3](https://doi.org/10.1016/S0082-0784(06)80338-3)

922 Santandrea, A., Bonamis, F., Pacault, S., Vignes, A., Perrin, L., Dufaud, O., 2019b. Influence  
 923 of the Particle Size Distribution on Dust Explosion: How to Choose the Right  
 924 Metrics? *Chemical Engineering Transactions* 77, 667–672.  
 925 <https://doi.org/10.3303/CET1977112>

926 Santandrea, A., Pacault, S., Perrin, L., Vignes, A., Dufaud, O., 2019a. Nanopowders  
 927 explosion: Influence of the dispersion characteristics. *Journal of Loss Prevention in*  
 928 *the Process Industries*. <https://doi.org/10.1016/j.jlp.2019.103942>

929 Shelkin, K.I., 1947. On Combustion in a Turbulent Flow [WWW Document]. *Journal of*  
 930 *Technical Physics*; Volume 13; No. 9-10. URL  
 931 <https://digital.library.unt.edu/ark:/67531/metadc64298/> (accessed 10.16.19).

932 Silvestrini, M., Genova, B., Leon Trujillo, F.J., 2008. Correlations for flame speed and  
 933 explosion overpressure of dust clouds inside industrial enclosures. *Journal of Loss*  
 934 *Prevention in the Process Industries* 21, 374–392.  
 935 <https://doi.org/10.1016/j.jlp.2008.01.004>

936 Skjold, T., 2007. Review of the DESC project. *Journal of Loss Prevention in the Process*  
 937 *Industries*, Selected Papers Presented at the Sixth International Symposium on

938 Hazards, Prevention and Mitigation of Industrial Explosions 20, 291–302.  
 939 <https://doi.org/10.1016/j.jlp.2007.04.017>

940 Skjold, T., 2003. Selected aspects of turbulence and combustion in 20-Litre explosion vessel  
 941 (Master thesis). University of Bergen, Norway.

942 Sundaram, D.S., Puri, P., Yang, V., 2013. Pyrophoricity of nascent and passivated aluminum  
 943 particles at nano-scales. Combustion and Flame 160, 1870–1875.  
 944 <https://doi.org/10.1016/j.combustflame.2013.03.031>

945 Tamanini, F., 1990. Turbulence effects on dust explosion venting. Plant/Operations Progress  
 946 9, 52–60. <https://doi.org/10.1002/prsb.720090111>

947 Tang, F.-D., Goroshin, S., Higgins, A., Lee, J., 2009. Flame propagation and quenching in  
 948 iron dust clouds. Proceedings of the Combustion Institute 32, 1905–1912.  
 949 <https://doi.org/10.1016/j.proci.2008.05.084>

950 Taveau, J., Lemkowitz, S.M., Hochgreb, S., Roekaerts, D., 2018. Scaling up the severity of  
 951 metal dusts deflagrations. Proceedings of the 12th International Symposium on  
 952 Hazards, Prevention and Mitigation of Industrial Explosions (XII ISHPMIE).

953 Taylor, G.I., 1922. Diffusion by Continuous Movements. Proceedings of the London  
 954 Mathematical Society 20, 196–212. <https://doi.org/10.1112/plms/s2-20.1.196>

955 Tolia, I.C., Venetsanos, A.G., 2018. An improved CFD model for vented deflagration  
 956 simulations – Analysis of a medium-scale hydrogen experiment. International Journal  
 957 of Hydrogen Energy 43, 23568–23584. <https://doi.org/10.1016/j.ijhydene.2018.10.077>

958 Torrado, D., 2017. Effect of carbon black nanoparticles on the explosion severity of gas  
 959 mixtures (PhD Thesis). Université de Lorraine, France.



960 Torrado, D., Buitrago, V., Glaude, P.-A., Dufaud, O., 2017a. Explosions of  
 961 methane/air/nanoparticles mixtures: Comparison between carbon black and inert  
 962 particles. *Process Safety and Environmental Protection* 110, 77–88.  
 963 <https://doi.org/10.1016/j.psep.2017.04.014>

964 Torrado, D., Cuervo, N., Pacault, S., Glaude, P.-A., Dufaud, O., 2017b. Influence of carbon  
 965 black nanoparticles on the front flame velocity of methane/air explosions. *Journal of*  
 966 *Loss Prevention in the Process Industries* 49, 919–928.  
 967 <https://doi.org/10.1016/j.jlp.2017.02.006>

968 Turkevich, L.A., Fernback, J., Dastidar, A.G., Osterberg, P., 2016. Potential explosion hazard  
 969 of carbonaceous nanoparticles: screening of allotropes. *Combustion and Flame* 167,  
 970 218–227. <https://doi.org/10.1016/j.combustflame.2016.02.010>

971 van der Wel, P.G.J., 1993. Ignition and propagation of dust explosions (PhD Thesis). Delft  
 972 University, The Netherlands.

973 van der Wel, P.G.J., van Veen, J.P.W., Lemkowitz, S.M., Scarlett, B., van Wingerden, C.J.M.,  
 974 1992. An interpretation of dust explosion phenomena on the basis of time scales.  
 975 *Powder Technology* 71, 207–215. [https://doi.org/10.1016/0032-5910\(92\)80010-T](https://doi.org/10.1016/0032-5910(92)80010-T)

976 Varea, E., 2013. Experimental analysis of laminar spherically expanding flames (thesis).  
 977 Rouen, INSA.

978 Vignes, A., 2008. Évaluation de l’inflammabilité et de l’explosivité des nanopoudres : une  
 979 démarche essentielle pour la maîtrise des risques (PhD Thesis). Institut National  
 980 Polytechnique de Lorraine, France.

981 Vignes, A., Krietsch, A., Dufaud, O., Santandréa, A., Perrin, L., Bouillard, J., 2019. Course of  
 982 explosion behaviour of metallic powders – From micron to nanosize. *Journal of*  
 983 *Hazardous Materials* 379, 120767. <https://doi.org/10.1016/j.jhazmat.2019.120767>

984 Wu, H.C., Wu, C.W., Ko, Y.H., 2014. Flame phenomena in nanogrinding process for titanium  
985 and iron. *J. Loss Prev. Process Ind.* 27, 114–118.

986 Zhen, G., Leuckel, W., 1997. Effects of ignitors and turbulence on dust explosions. *Journal of*  
987 *Loss Prevention in the Process Industries* 10, 317–324. [https://doi.org/10.1016/S0950-](https://doi.org/10.1016/S0950-4230(97)00021-1)  
988 [4230\(97\)00021-1](https://doi.org/10.1016/S0950-4230(97)00021-1)

989